

# Review of Physics and Monte Carlo Techniques as Relevant to a Cryogenic, Phonon and Ionization Readout, Radiation-Detector

Steven W. Leman\*

*Kavli Institute for Astrophysics and Space Research,  
Massachusetts Institute of Technology, Cambridge, MA 02139, USA*

This review discusses detector physics and Monte Carlo techniques for cryogenic, radiation detectors that utilize combined phonon and ionization readout. Particular focus is placed on instrumentation that is used in the Cryogenic Dark Matter Search detectors however the discussion is quite general and includes phonon and charge transport physics relevant at low temperatures. Sufficient tutorials and physics references are provided such that an interested reader can jump right into a detector Monte Carlo campaign.

## Contents

<b>I. Introduction</b>	2
<b>II. Radiation Modeling</b>	3
<b>III. Phonon Simulation</b>	4
A. Introduction	4
B. Slowness Surfaces / Phase Velocities and Polarization Vectors	4
C. Group Velocities	5
D. Anisotropic Isotope Scattering	7
E. Anharmonic Decay	7
1. General Case	7
2. Isotropic Approximation	8
F. Phonon Losses at Surfaces	11
G. Time Steps	11
H. Random Number Sampling	12
I. Numerical Constants for Phonon Simulations	12
<b>IV. Quasiparticle Down Conversion</b>	12
A. MC process ordering	14
<b>V. Charge MC</b>	14
A. Introduction	14
B. Holes: propagation and scattering with isotropic bands and isotropic phonon velocity	15
C. Electrons: propagation and scattering with anisotropic bands and isotropic phonon velocity	17
D. Time steps	17

---

\*Electronic address: swleman@mit.edu

E. Select constants for charge Monte Carlo	18
<b>VI. Electric-Field Lookup</b>	18
A. Electric-Field Lookup from Triangulated Mesh	18
B. Barycentric Coordinates	19
C. Barycentric Coordinate Formulae	19
D. Barycentric Coordinate Procedures and Shortcuts in the DMC	21
E. Determining if a Charge Leaves a Triangle	22
<b>VII. Transition Edge Sensor Simulations</b>	22
A. Introduction	22
B. Electrical Circuit Modeling	23
1. TES Voltage Modeling	26
C. Thermal Processes	27
D. Parsing Phonons Into The TESs	30
<b>VIII. Final Remarks</b>	32
<b>Acknowledgments</b>	32
<b>References</b>	32

## I. INTRODUCTION

Cryogenic radiation-detectors that utilize ionization, phonon and / or scintillation measurements are being used in a number of experiments. Both the Cryogenic Dark Matter Search (CDMS) [1, 2] and EDELWEISS [3] dark matter search utilize germanium targets to detect recoils of radiation in germanium target masses. A combination of ionization and phonon readout is used to provide discrimination of gamma and neutron recoil types. The CRESST dark matter search utilizes  $\text{CaWO}_4$  targets and readout scintillation and phonon signal to discriminate between recoil type. The advantage of reading out both phonon and ionization (or scintillation) signals comes about from the differing ratios of ionization and phonon energy or scintillation and phonon energy created in electron and nuclear recoils in the detectors. The ratio of these two energies leads to a powerful discriminator for the experiment's desired recoil type.

Both the ionization and phonon readout can be used to generate position estimators for the initial radiation interaction, leading to fiducial volume selection. In the ionization signal this is generally accomplished by instrumenting different parts of the detector with independent readout channels and vetoing events with large signal contribution outside of the desired fiducial volume. In the phonon signal it is generally required to measure the early, athermal component of the phonon signal which still retains a position dependent component.

The physics required to accurately model these detectors is presented in this paper along with appropriate numerical tricks that are useful for an efficient detector Monte Carlo. This paper proceeds with a review of radiation interactions, charge transport physics, phonon transport physics, instrumentation. Monte Carlo techniques and relevant physical constants are included where appropriate.

This paper will focus on the use of silicon and germanium detector masses, both of which are group IV semiconductors. However there are other relevant materials in use such as calcium tungstate ( $\text{CaWO}_4$ ) which leads to a small loss of generality.

## II. RADIATION MODELING

When using a Monte Carlo of a detector, it is often helpful or necessary to have a numerical model of radiation interactions in the detector. Many readers will find it valuable to use separate modeling software such as GEANT4 [4] so the details of these interactions can remain left out from this paper. It is useful still to have a sense of various interactions types.

Low energy gamma-rays (x-rays) predominantly interact via photoelectric absorption in which all of the gamma-ray energy is deposited in a single interaction location. High energy gamma-rays interact via Compton scattering in which some of the gamma-ray's initial energy is transferred to an electron and the gamma-ray continues along a different trajectory with reduced energy. The gamma-ray will generally continue to scatter until it leaves the detector volume or terminates with a photoelectric absorption. In silicon (germanium), for photon energies greater than 60 (160) keV, Compton scattering dominates [5, 6].

Both of these electron interactions result in a high energy electron being produced which then undergoes a rapid cascade process resulting in a large number of electron hole pairs [6, 7]. This initial cascade process ceases around the scale of the mean electron-hole pair creation energy ( $E_{eh,create}$ ) resulting in an expected number of electron hole pair  $n_{eh} = E_{\gamma}/E_{eh,create}$ . Due to correlations in the cascade process, the variance in the number of electron hole pairs is reduced, relative to Poisson statistics, and given by  $\sigma_{eh}^2 = F \times n_{eh}$ , where  $F$  is the Fano factor [8]. These high energy electron-hole pairs will then shed phonons until they reach the semiconductor gap energy  $E_{gap}$  which results in the fraction  $1 - E_{gap}/E_{eh,create}$  of energy in prompt phonons and the remainder in the electron-hole pair system.

Neutrons that interact in the detector bulk will knock an ion out of its lattice site and displace it to some other location in the crystal. This high energy ion will then interact with both the lattice ions and / or valence electrons with competing cross sections. Interactions with the lattice ions can be described to first approximation as Rutherford scattering [9] with differential energy loss per unit length  $-dE/dx \sim v^{-2}$ , where  $v$  is the ion's velocity [10]. For interactions with valence electrons, only electrons with velocity  $v$  within the Fermi surface can be excited by the ion and hence the differential energy loss per unit length scales like  $-dE/dx \sim v$ . There are important screening and velocity dependent cross sections in both energy loss lengths but to first approximation these equations show the velocity dependent competition in the two scattering rates. Which ever interaction occurs first, there is generally a cascade of many scatters resulting in a larger amount of energy being deposited in the ion lattice compared to gamma-ray interactions. For historical reasons, the reduced amount of energy in the electron-hole (ionization) system, compared to an equal energy deposition by a gamma-ray, has brought about the term *nuclear quenching* to describe the reduced ionization signal. The details of the cascade and reduction in the number of electron hole pairs is described by Lindhard theory [11] and given as  $f = kg(\epsilon)/(1 + kg(\epsilon))$  where  $\epsilon = 11.5E_R Z^{-7/3}$ ,  $k = 0.133Z^{2/3}A^{-1/2}$  and  $g(\epsilon) = 3\epsilon^{0.15} + 0.7\epsilon^{0.6} + \epsilon$  [12]. The recoil energy is  $E_R$  and given in units of keV,  $Z$  is the atomic number and  $A$  is the atomic mass.

Beta radiation represents another class of electron-recoil interactions. The attenuation lengths are much shorter however resulting in a class of events sometimes referred to as *surface interactions*. These surface interactions can result in signals that differ from bulk events of the same energy and electron / nuclear recoil type. For example, the events may be located in regions of large electric fringing fields, directing charges away from readout electrodes or near mounting hardware that absorbs scintillation light.



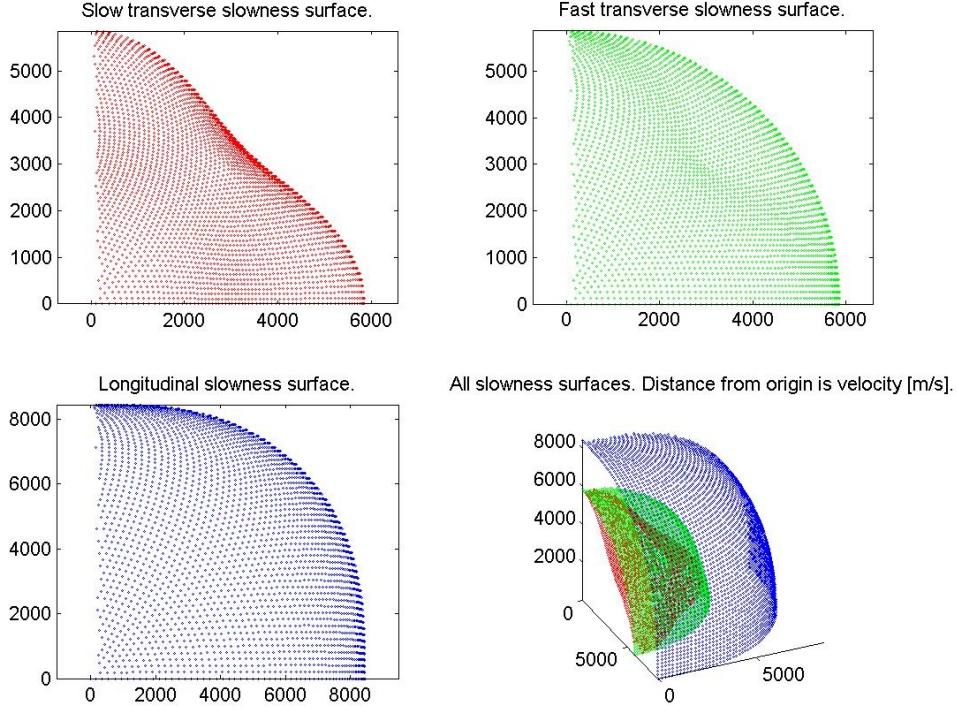


FIG. 1: Slowness surfaces in silicon. These are found by solving for the eigenvalues in Equation 3. The distance from the origin represents the phase velocity speed (in m/s). Silicon’s cubic crystal geometry leads to them being non-spherical. The first three plots are views from the north pole. The fourth view containing all three surfaces is offset from the north pole. In the plots all modes are equally populated, which does not reflect the actual mode populations.

The eigenvectors represent the three polarization vector directions and the three eigenvalues equal  $\rho\omega^2$  for the longitudinal, slow-transverse and fast-transverse modes. The anisotropy in the cubic silicon crystal leads to the slowness surfaces being non-spherical (see Figure 1). The slowness surfaces are used to determine both the group velocities (Section III C) and also the isotope scattering rates.

### C. Group Velocities

Phonon group velocities are found by solving

$$\vec{v}_g(\theta, \phi) = \frac{\partial\omega(\theta, \phi)}{\partial\vec{k}}.$$

The slight lack of sphericity in the slowness surfaces (see Figure 1) has a very dramatic effect

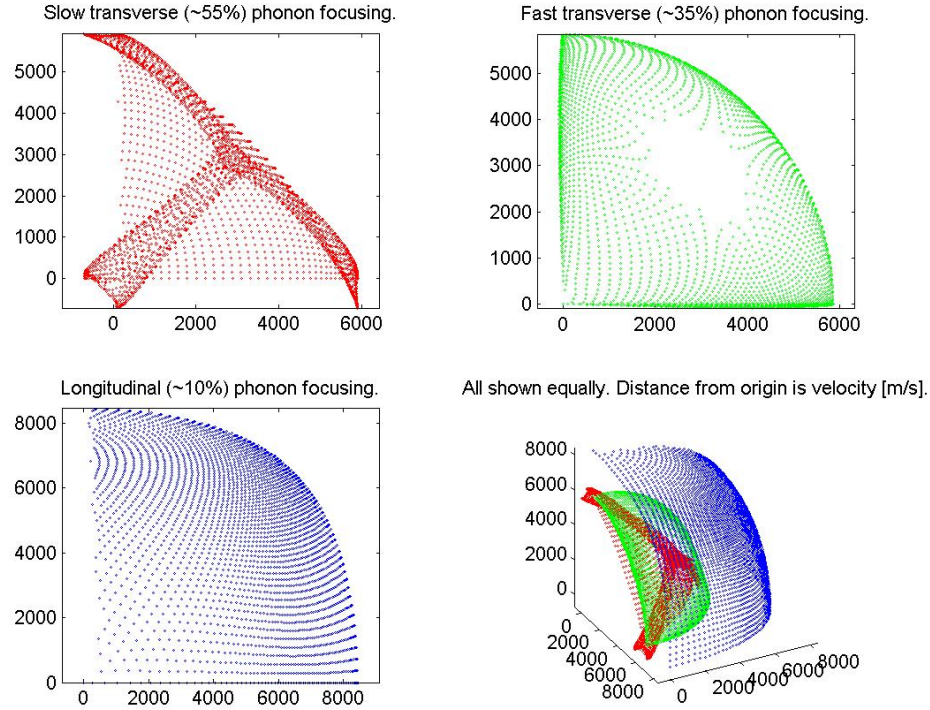


FIG. 2: Group velocities in silicon. The slight lack of sphericity in the slowness surfaces (see Figure 1) has a very dramatic effect on the transverse phonon group velocities. The longitudinal phonon group velocity is only mildly impacted. Energy is focused in the direction of heavy banding and leads to the term *phonon focusing*. The distance from the origin represents the speed that phonon energy is carried through the crystal (in m/s). In the plots all modes are equally populated, which does not reflect the actual mode populations.

on the transverse phonon group velocities [16–19] (see Figure 2). The longitudinal phonon’s group velocity is only mildly affected. Energy is focused in the direction of heavy banding and leads to the term *phonon focusing*. The distance from the origin represents the speed that phonon energy is carried through the crystal.

The point density in the plots is misleading as the three modes are shown to be equally populated. Isotope scattering (see Section III D) leads to the phonon modes being populated as follows: slow-transverse (55%), fast-transverse (35%) and longitudinal (10%).

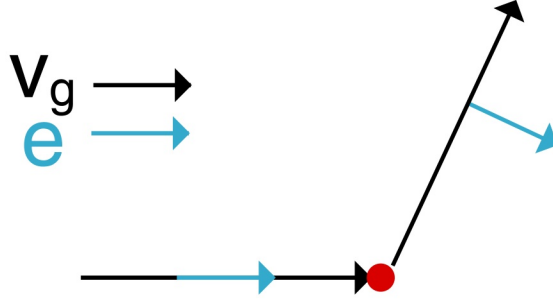


FIG. 3: Phonons isotope scatter off mass defects in the crystal. Equation III D gives the individual phonon scatter rates.  $v_g$  is the group velocity and  $\vec{e}$  is the polarization vector.

#### D. Anisotropic Isotope Scattering

Phonons scatter off mass defects in the crystal (see Figure 3). Additionally, they can change modes. The bulk scattering rate is given by

$$\Gamma_I = B\nu^4[s^3],$$

where  $\nu$  is the phonon frequency and  $B$  is a scattering rate constant [17, 19–22] (see Section I). The scattering rate for individual phonons is given by

$$\gamma \sim \frac{|\vec{e}_\lambda \cdot \vec{e}_{\lambda'}|^2}{\nu_{\lambda'}^3},$$

where  $\nu$  is the phonon frequency in Hz,  $\vec{e}$  is the polarization vector,  $\lambda$  represents the initial phonon and  $\lambda'$  represents the outgoing phonon [19, 22]. It is the dot product in Equation III D which allows mode mixing and the denominator which ensures the correct populations in the ratios slow-transverse (55%), fast-transverse (35%) and longitudinal (10%). The standard treatment is to determine if a phonon isotope scatters via  $\Gamma_I$  and then determine its polarization and direction via  $\gamma$ . After the initial anharmonic decay has settled down, isotope scattering dominates.

This process is unfortunately computationally expensive due to sample-rejection techniques [23] and after several iterations an isotropic scattering process can be used for individual phonons with little loss of modeling accuracy.

#### E. Anharmonic Decay

##### 1. General Case

Nonlinear terms in the elastic coupling constants cause a longitudinal phonon to down convert to two lower energy phonons (see Figure 4). The bulk decay rate is given by

$$\Gamma_A = A\nu^5[s^4],$$

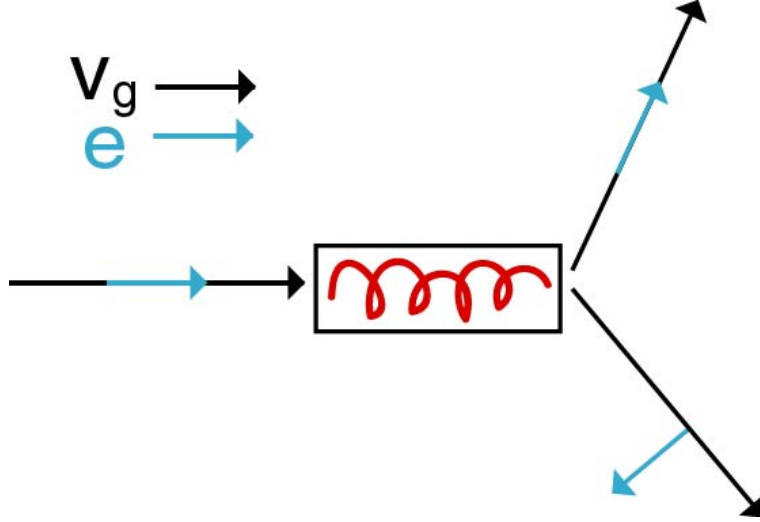


FIG. 4: Longitudinal phonons decay due to nonlinear terms in the elastic coupling constants.  $\vec{v}_g$  is the group velocity and  $\vec{e}$  is the polarization vector.

where  $\nu$  is the phonon frequency and  $A$  is a decay rate constant [19–22] (see Section I). The decay rate for transverse phonons is negligible [24]. The three body problem requires that both energy and momentum are conserved. These conditions make an exact solution computationally prohibitive for large amounts of phonons.

## 2. Isotropic Approximation

To allow computations to proceed in a finite time, an exact solution to anharmonic decay was abandoned and an isotropic approximation is used. The energy distribution calculations are still difficult but fortunately have already been carried out [25, 26]. Once the energies have been determined, calculating the resultant scattering angles based on energy and momentum conservation is fairly straight forward. The  $L \rightarrow L' + T'$  energy distribution is given by

$$\Gamma_{L \rightarrow L' + T'} \sim \frac{1}{x^2} (1 - x^2)^2 [(1 + x)^2 - \delta^2(1 - x)^2] [1 + x^2 - \delta^2(1 - x)^2]^2,$$

where  $x = E_{L'}/E_L$ ,

$\delta = \frac{v_l}{v_t}$  and,

$\frac{\delta-1}{\delta+1} < x < 1$ .

This approximation results in the outgoing phonons having an angular displacement from the initial phonon given by

$$\cos(\theta_{L'}) = \frac{1 + x^2 - \delta^2(1 - x)^2}{2x},$$

$$\cos(\theta_{T'}) = \frac{1 - x^2 + \delta^2(1 - x)^2}{2\delta(1 - x)}.$$

The  $L \rightarrow T' + T'$  energy distribution is given

$$\Gamma_{L \rightarrow T'_1 + T'_2} \sim (A + B\delta x - Bx^2)^2 + \left[ Cx(\delta - x) - \frac{D}{\delta - x} \left( x - \delta - \frac{1 - \delta^2}{4x} \right) \right]^2,$$

where  $x = \delta \frac{E_{T'_1}}{E_L}$ ,

$$\delta = \frac{v_l}{v_t},$$

$$\frac{\delta-1}{2} < x < \frac{\delta+1}{2},$$

$$A = \frac{1}{2}(1 - \delta^2)[\beta + \lambda + (1 + \delta^2)(\gamma + \mu)],$$

$$B = \beta + \lambda + 2\delta^2(\gamma + \mu),$$

$$C = \beta + \lambda + 2(\gamma + \mu) \text{ and,}$$

$$D = (1 - \delta^2)(2\beta + 4\gamma + \lambda + 3\mu).$$

This approximation results in the outgoing phonons having an angular displacement from the initial phonon given by Equations 5 and 6.

$$\cos(\theta_{T'_1}) = \frac{1 - \delta^2(1 - x)^2 + \delta^2 x^2}{2\delta x}, \quad (5)$$

$$\cos(\theta_{T'_2}) = \frac{1 - \delta^2 x^2 + \delta^2(1 - x)^2}{2\delta(1 - x)}. \quad (6)$$

Where the trivial substitution  $x \rightarrow 1 - x$  is made for the second phonon. With these closed-form energy densities and scattering angles, plots can be generated to aid understanding of these events (see Figures 5 and 6).

These angles are relative the present momentum vector  $\vec{k}$  and need to be converted into the MC coordinate system. Polar coordinates are useful and angles are provided in this system. In addition to rotation angles  $\theta_{L'}$  and  $\theta_{T'}$  (or  $\theta_{T'_1}$  and  $\theta_{T'_2}$ ) an additional azimuth angle, relative to  $\vec{k}$  and randomly distributed from  $[0, 2\pi]$  must be specified  $\theta_{2\pi}$ .

In terms of initial elevation and azimuth angles  $\Phi$  and  $\Theta$ , scattering angles  $\theta_{T'_1}$  and  $\theta_{T'_2}$  and azimuth scattering angle  $\theta_{2\pi}$ , the final angles  $\Phi_1, \Theta_1$  for  $\vec{k}_1$  are

$$\Phi_1 = \arccos[-\sin \Phi \sin \theta_{T'_1} \cos \theta_{2\pi} + \cos \Phi \cos \theta_{T'_1}]$$

$$\Theta_1 = \Theta - \arctan 2[-\sin \theta_{T'_1} \sin \theta_{2\pi} \sin \Phi, \cos \theta_{T'_1} - \cos \Phi \cos \Phi_1].$$

The final angles  $\Phi_2, \Theta_2$  for  $\vec{k}_2$  are found by replacing  $\theta_{T'_1}$  with  $\theta_{T'_2}$  and  $\theta_{2\pi}$  with  $2\pi - \theta_{2\pi}$ .

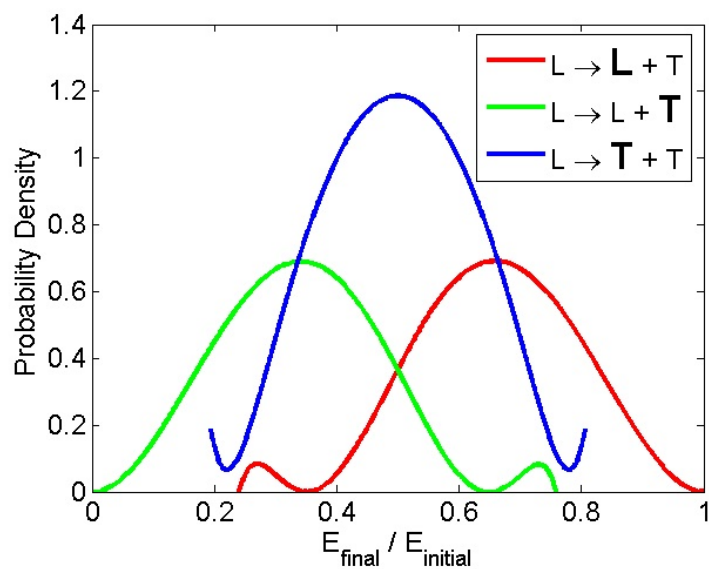


FIG. 5: Resultant energies in longitudinal phonon decay in germanium. The two branches  $L \rightarrow L+T$  and  $L \rightarrow T+T$  are shown; the plotted distribution is indicated in bold face in the legend.

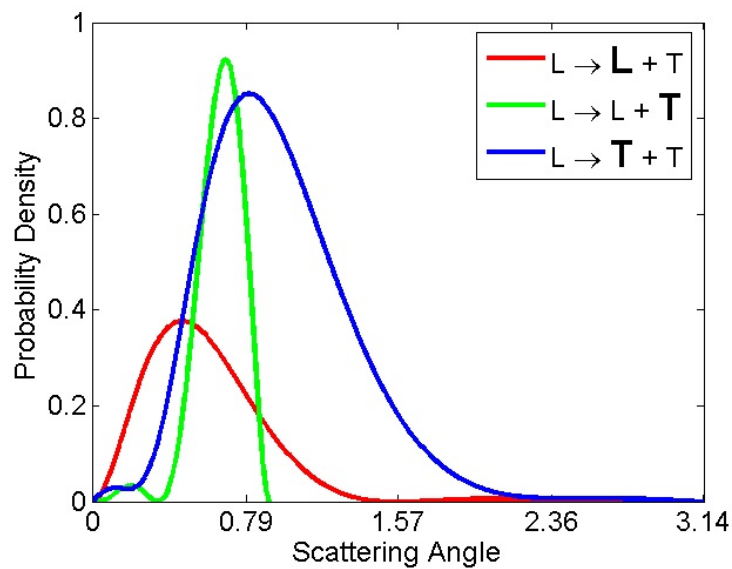


FIG. 6: Resultant angles in longitudinal phonon decay in germanium. The two branches  $L \rightarrow L+T$  and  $L \rightarrow T+T$  are shown; the plotted distribution is indicated in bold face in the legend.

## F. Phonon Losses at Surfaces

Eventually the phonons will interact at surfaces where they are instrumented, reflect, down convert or are lost to the environment.

Phonons can reflect either specularly or diffusively from the surfaces. Specular reflection can occur on smooth, untreated semiconductor wafer surfaces. It is the simplest to describe with incident and reflected angles relative to the normal equal,  $\theta_i = \theta_r$ .

Diffusive scattering is also common on surfaces that have been damaged or roughened during fabrication. In the ideal case the scattering angle is described by Lambert's cosine law where the angular distribution scales like  $\cos\theta$  where the angle  $\theta$  is measured relative to the normal. Scattering surfaces that satisfy Lambert's cosine law scatter phonons isotropically regardless of their incident angle. Generally diffusive scattering has been found to be a good model for phonon-surface reflections, likely due to some small roughness in the surface.

Phonons are strictly-speaking eigenstates of a Hamiltonian that describes an infinitely large, periodic lattice. This description necessarily breaks down at the detector surfaces and there is some probability that phonons down convert to lower energy daughters at the surface. The details of this process would be highly material / surface treatment dependent but the probability of this occurring for a particular phonon-surface interaction will be small for a high purity crystal. It is generally easiest to tune this probability by running numerous MC to find the best value.

It is the goal of the experimental setup to absorb the phonons into some sensor and provide instrumentation into a data acquisition system. The details for the phonon-sensor interaction probability are again complicated and highly depend on the type of absorber and attachment / fabrication details. Acoustic mismatch theory provides a good starting point for analytic calculations and can be performed over both normal and non-normal incidence angles. The relevance of these calculations can be lost however when detector to detector variations are considered. Additionally the angular dependence of such calculations can be washed out when integrating over a distribution of phonon incident angles. In practice it is usually again easiest to tune this probability by running numerous MC and identifying the best fit value. For any well designed detector, phonon absorption into the instrumentation sensors will dominate over other loss processes allowing the probability to be tuned by matching pulse decay times.

## G. Time Steps

It would be grossly inefficient to run all phonons with the same time step. Therefore we generate scattering times according to the distributions in Sections III D and III E. The scattering and decay probabilities go like  $P = 1 - \exp(-t/\tau)$  where  $\tau$  is a combination of isotope scattering and anharmonic decay rates as given by Matthiessen's rule  $1/\tau = 1/\tau_{iso} + 1/\tau_{anh}$ .

This scattering time has to be compared with the time that the phonon will take to interact with a surface and the event that occurs soonest will be chosen for each individual phonon. If it is determined that the bulk interaction time is less than the surface interaction time, then it must be determined which event occurs based on their relative, frequency dependent rates. This can be done by drawing a uniform random number  $u$  and comparing to the rate of the process in question to the total rate. For example, if  $u < (1/\tau_{anh})/(1/\tau_{anh} + 1/\tau_{iso})$  then an anharmonic decay is selected.

## H. Random Number Sampling

Only in rare circumstances will a uniform random number  $u$  be needed in MC without some transformation. Often we are trying to draw the number  $x$  out of the probability distribution function (PDF)  $f$ . An efficient method for transforming  $u$  to the desired probability distribution function  $f$  is to integrate  $f$  to find the cumulative distribution function  $F = \int f$ . The cumulative distribution function (CDF)  $F$  has the desirable property that it is bounded by  $[0, 1]$  as is  $u$ . The CDF  $F$  is then inverted and solved at  $u$  to determine  $f$ ,  $x = F^{-1}(u)$  [23].

As an example, we first considering the bulk interaction rate where the probability of having an interaction is  $P = 1 - \exp(-t/\tau)$ . After integration and inversion, the randomly generated scattering time and is given by

$$t_{scatter} = -\tau \ln(u).$$

As a second example we can consider diffuse scattering off the detector walls. In a spherical coordinate system where  $\theta$  represents the angle from the surface normal, the PDF in this coordinate is  $f = \sin(\theta)$ . This is also easily integrated and inverted to yield  $F^{-1} = \arccos(u)$ . Care must be taken in this example however since arccos is defined over the domain  $[-1, 1]$  which modifies to  $F^{-1} = \arccos(2u - 1)$ .

There are times when a PDF cannot be analytically integrated to yield a CDF or the CDF cannot be inverted. This is an unfortunate situation since an expensive rejection technique is required. This technique involves drawing a pair of uniform random numbers  $[u_x, u_y]$  where  $\min(x) \leq u_x \leq \max(x)$  and  $\min(f) \leq u_y \leq \max(f)$ . If  $u_y < f(u_x)$  then  $u_x$  is retained, otherwise  $u_x$  is rejected and the process is repeated. The inefficiency of this method is related to the area coverage  $c = \int f(x)dx / (\max(f) \times (\max(x) - \min(x)))$  and  $u_x$  will be successfully drawn in one of  $c$  attempts.

The rejection method can be improved however for *static* distributions that do not change during the MC run. An example includes diffusive scattering off of the side walls of the detector when using a spherical coordinate system. In this case, the  $\sin(\theta)$  Jacobian results in the PDF  $f = \sin(\theta)^2$  for which  $F$  cannot be found analytically. The PDF can be integrated numerically to generate a CDF which is subsequently inverted. The process lacks a certain degree of elegance but is significantly more efficient than using a rejection method.

## I. Numerical Constants for Phonon Simulations

Table III lists numerous constants that are used in the phonon simulations. They define the propagation dynamics, scattering and decay rates and energy carrier statistics.

## IV. QUASIPARTICLE DOWN CONVERSION

Phonons have some probability of entering and interacting in the thin aluminum films that are patterned on the surface. These aluminum films make up both the phonon collecting films and ionization ground lines; it is interactions in the former that are measured in the phonon sensors. If the phonons have energy greater than or equal than twice the superconducting gap  $E_\phi > 2E_g = \Delta$  then Cooper pairs can be broken creating two quasiparticles. These quasiparticles will be of high kinetic energy  $E_{kinetic} = E_\phi - \Delta$  and contain some probability of scattering off phonons. These daughter phonons thereby introducing a population of downconverted phonons back into the metal

TABLE I: Numerical Constants for Phonon Simulations

Parameter Description	Symbol	Units	Silicon	Germanium	Reference
Isotope Scatter Rate	$(B)$	$[\text{s}^3]$	$2.43 \times 10^{-42}$	$3.67 \times 10^{-41}$	[25]
Anharmonic Decay Rate	$(A)$	$[\text{s}^4]$	$7.41 \times 10^{-56}$	$6.43 \times 10^{-55}$	[25]
Longitudinal Velocity	$(v_l)$	$[\text{m/s}]$	9000	5310	[25]
Transverse Velocity	$(v_t)$	$[\text{m/s}]$	5400	3250	[25]
Decay Rate Constant	$(\beta)$		-0.429	-0.732	[25]
Decay Rate Constant	$(\gamma)$		-0.945	-0.708	[25]
Decay Rate Constant	$(\lambda)$		0.524	0.376	[25]
Decay Rate Constant	$(\nu)$		0.680	0.561	[25]
Density	$(\rho)$	$[\text{g/cm}^3]$	2.33	5.32	[25]
Decaying Ratio $\frac{L \rightarrow L+T}{\text{All Longitudinal Decays}}$			0.204	0.260	[25]
Lattice Constant	$(C_{11})$		1.66	1.29	[14]
Lattice Constant	$(C_{12})$		0.64	0.48	[14]
Lattice Constant	$(C_{44})$		0.80	0.67	[14]
Debye Frequency	$(\nu_D)$	$[\text{1/s}]$	$1.5 \times 10^{13}$	$0.864 \times 10^{13}$	[14]
Electron-Hole Energy		$[\text{eV}]$	1.17	0.75	[14]
Mean Electron-Hole Creation Energy		$[\text{eV}]$	3.81	2.96	[27]

film. These phonons could break additional Cooper pairs in a cascade process that ceases when all phonons have energy below  $\Delta$  or have a probability of being reintroduced back into the crystal. The key points in the cascade process are summarized in the following list [28–30].

1. Quasiparticle recombination lifetimes are long compared to quasiparticle decay and quasiparticle absorption into the aluminum films and therefore the recombination processes can be ignored.
2. Quasiparticle decay via absorption of a phonon is suppressed at low temperatures due to a phonon density of states term  $n(\Omega)$ , where  $\Omega$  is the phonon energy, in the Green's function and therefore can be ignored.
3. Quasiparticle decay via emission of a phonon results in phonons with an energy distribution given by  $P_\phi(\Omega) = \Omega^2 \rho(E - \Omega) \left(1 - \frac{\Delta^2}{E(E - \Omega)}\right)$ , where  $E$  is the quasiparticle energy and the quasiparticle density of states at temperature  $T=0$  goes like  $\rho(E) = \frac{E}{\sqrt{E^2 - \Delta^2}}$  and  $0 \leq \Omega \leq E$ .
4. Phonons break Cooper pairs producing quasiparticles with an energy distribution given by  $P_{QP}(E) = \left(1 + \frac{\Delta^2}{E(\Omega - E)}\right) \rho(E) \rho(\Omega - E)$ , where  $\Delta \leq E \leq \Omega - E$ . The phonon is completely absorbed so that the second quasiparticle has energy  $E_2 = \Omega - E$ .

5. Phonons are lost to the crystal if they reach the aluminum / crystal interface.

### A. MC process ordering

In the physical processes can be ordered as follows

1. If the phonon energy is sufficient  $\Omega > 2 \times E_{gap}$ , a quasiparticle pair is created with the distribution  $P_{QP}(E)$  previously described.
2. If there is a quasiparticle with energy  $E \geq 3 \times E_{gap}$  then the quasiparticle emits a phonon with energy distribution  $P_{\phi}(\Omega)$ . Quasiparticles with energy  $E < 3 \times E_{gap}$  provide an endpoint for quasiparticle generation and can be removed from the MC.
3. The probability of a phonon escaping the crystal is a function of the distance to reach the aluminum / crystal interface and the phonon / Cooper pair interaction length. Given the large number of phonons it is generally not necessary to track this process in detail and instead a simple model is sufficient. On average, phonons are assumed to populate the center of the aluminum film ( $z = l_{Al}/2$ ), where  $l_{Al}$  is the aluminum thickness, and the phonons have 1/2 probability of traveling upwards and 1/2 probability of traveling downwards. For the downward going phonons there is an  $exp(-(2 \times l_{Al}/2)/L_0)$  probability of reaching the aluminum / crystal interface before scattering, where  $L_0 \sim 720 \text{ nm}$  is a characteristic phonon interaction length [30]. The factor of  $2 \times$  is provided to integrate over different phonon incidence angles. The factor  $l_{Al}/2$  is replaced by  $l_{Al} \times 3/2$  for upward going phonons.
4. If the phonon has not been removed from Monte Carlo in step 2 or reintroduced into the crystal in step 3 then the process repeats at step 1.

## V. CHARGE MC

### A. Introduction

Accurate modeling of charge propagation is included in Monte Carlo for numerous reasons. First, the ionization signal, compared to the phonon signal, provides a discriminator between electron-recoil and nuclear-recoil events in the silicon and germanium detectors. Second, electron transport is described by a mass tensor, leading to electron transport which contains components oblique to the applied field<sup>6,7</sup> and is necessary to explain and interpret signals in the primary and guard-ring ionization channels which function as a fiducial volume cut [31, 32]. Third, charges drifting through the detector produce a population of phonons which contribute 42% of the total phonon signal at  $\pm 3 \text{ V}$  bias. These phonons' spatial, time, energy and emitted-direction distributions should therefore be properly modeled in Monte Carlo of the detector response. Fourth, phonons created during electron-hole recombination at the surfaces contribute 14% of the total phonon signal but in a low frequency, ballistic regime that is used to provide a surface-event discriminator. These phonons also need to be properly modeled in a Monte Carlo.

Germanium has an anisotropic band structure described schematically in Figure 7 and shows energy band structure in which the hole ground state is situated in the  $\Gamma$  band's [000] direction and the electron ground state is in the L-band [111] direction. Hole propagation dynamics are relatively simple due to propagation in the  $\Gamma$  band and the isotropic energy-momentum dispersion

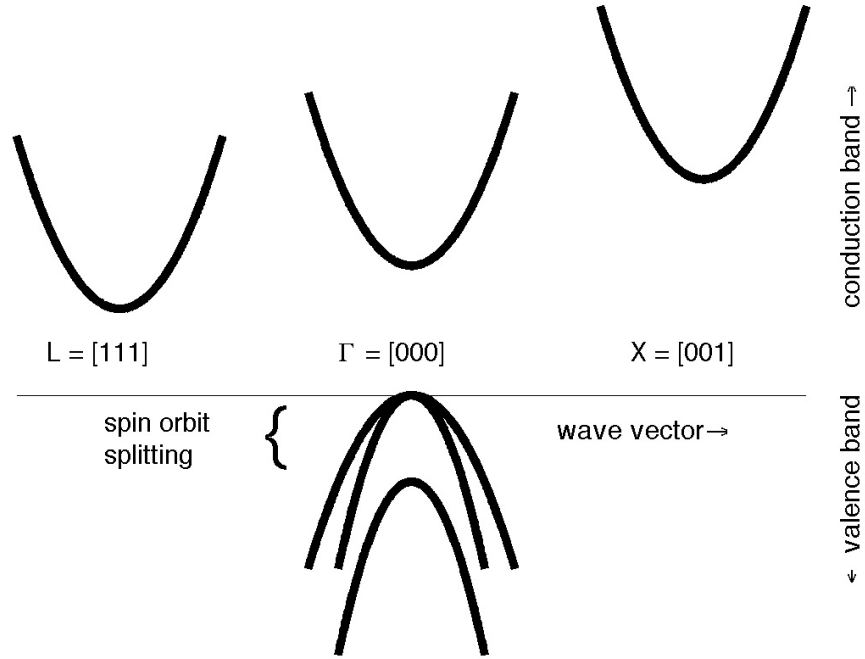


FIG. 7: Energy band structure of germanium, showing the L-valleys at  $\langle 111 \rangle$ , the  $\Gamma$  valley at  $\langle 000 \rangle$ , and the X-valley at  $\langle 100 \rangle$ . Symmetry results in 8 total L-valleys and 6 total X-valleys.

relationship  $\epsilon(\vec{k}) = \hbar^2 k^2 / 2m$ . Electron propagation dynamics are significantly more complicated due to the band structure and anisotropic energy-momentum relationship. At low fields and low temperatures, electrons are unable to reach sufficient energy to propagate in the  $\Gamma$  or X-bands, and are not considered necessary to consider in Monte Carlo. The electron energy-momentum dispersion relationship is given by  $\epsilon(\vec{k}) = (\hbar^2 / 2) \times (k_{\parallel}^2 / m_{\parallel} + k_{\perp}^2 / m_{\perp})$ , where the longitudinal and transverse mass ratio  $m_{\parallel} / m_{\perp} \sim 19.5$ .

This chapter will proceed by describing hole propagation and scattering, electron propagation and scattering utilizing a Herring-Vogt transformation and finally electron-hole recombination.

### B. Holes: propagation and scattering with isotropic bands and isotropic phonon velocity

Hole propagation dynamics are described by momentum evolution in an electric field  $\hbar \frac{d\vec{k}}{dt} = e\vec{E}$  and propagation in position space  $\vec{v} = \hbar \vec{k} / m_c$ , where  $m_c$  is the effective carrier mass.

Charge carriers cannot accelerate indefinitely however, and the shedding of Neganov-Luke

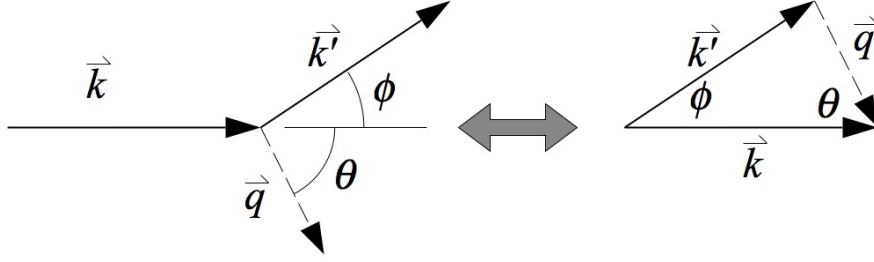


FIG. 8: Electron with initial wave vector  $\vec{k}$  and final wavevector  $\vec{k}'$  scattering off of lattice at angle  $\phi$  with respect to  $\vec{k}$  and emitting a phonon with wavevector  $\vec{q}$  at angle  $\theta$  with respect to  $\vec{k}$ , where the vector momenta sum as shown on right.

phonons [33, 34] limits their speed to around the longitudinal phonon phase velocity  $v_L$ . As described in Figure 8, charge-phonon scattering is an elastic processes, conserving both momentum  $\vec{k} - \vec{k}' = \vec{q}$  (where  $\vec{k}$  and  $\vec{k}'$  are the initial and final hole momentum vectors and  $\vec{q}$  is the phonon momentum vector) and energy  $\epsilon - \epsilon' = \hbar\omega$  (where  $\epsilon$  and  $\epsilon'$  are the initial and final hole energies and  $\hbar\omega$  is the phonon energy). The phonon energy-momentum dispersion relationship is given by  $\hbar\omega = v_L q$ . Due to the low carrier energy, Umklapp processes are suppressed.

Energy-momentum conservation coupled with the previous dispersion relationships leads to the final states  $k'^2 = k^2 + q^2 - 2kq \cos(\theta)$  and  $q = 2(k \cos \theta - k_L)$  and

$$\cos(\phi) = \frac{k^2 - 2k_s(k \cos \theta - k_s) - 2(k \cos(\theta) - k_s)^2}{k\sqrt{(k^2 - 4k_s(k \cos(\theta) - k_s))}},$$

where  $\theta$  is the angular displacement between  $\vec{k}$  and  $\vec{q}$ ,  $\phi$  is the angular displacement between  $\vec{k}$  and  $\vec{k}'$ , and  $k_L$  is defined as  $k_L = mv_L/\hbar$ . If we can determine a scattering rate  $\tau$  and phonon angular displacement  $\theta$ , then we can use these formulae to find the final states.

Fermi's Golden Rule provides the transition probability per unit time per unit energy as

$$P_{k,k'\pm q} = \frac{2\pi V}{\hbar} \left| \langle \vec{k} \pm \vec{q} | H | \vec{k} \rangle \right|^2 \delta(E - E' \mp \hbar\omega).$$

For phonon emission processes,

$$\left| \langle \vec{k} \pm \vec{q} | H | \vec{k} \rangle \right|^2 = \frac{C^2 \hbar}{2V \rho v_L} q(n_q + 1),$$

where  $C$  is the deformation potential constant. A characteristic length can be defined as  $l_0 = \frac{\pi \hbar^4 \rho}{2m^3 C^2}$ . The transition probability can be integrated over  $\theta$  and  $E'$  to obtain a scattering rate

$$1/\tau = \frac{1}{3} \frac{v_L}{l_0} \frac{k}{k_L} \left[ 1 - \frac{k_L}{k} \right]^3.$$

The angular distribution then follows to be

$$P(k, \theta)d\theta = \frac{v_L}{l_0} \left(\frac{k}{k_L}\right)^2 \left(\cos(\theta) - \frac{k_L}{k}\right)^2 \sin \theta d\theta \quad (7)$$

where  $0 \leq \theta \leq \arccos(\sqrt{k_l/k}) < \pi/2$ .

The phonon scatter azimuthal rotation angle is uniformly distributed about  $0 \leq \vartheta \leq 2\pi$ . The charge carrier azimuthal rotation angle is required to be  $\varphi = \pi + \vartheta$ .

### C. Electrons: propagation and scattering with anisotropic bands and isotropic phonon velocity

Electron propagation and scattering is complicated by the anisotropy of the electron bands but can be simplified by performing first a transformation into a space defined by the vectors  $(\vec{e}_{\parallel}, \vec{e}_{\perp 1}, \vec{e}_{\perp 2})$  (where  $\vec{e}_{\parallel}$  is aligned with [111] and the other two are perpendicular) and then a Herring-Vogt transformation into a space where the electron bands are isotropic [32, 35]. The Herring-Vogt transformation is non-unitary and in the  $(\vec{e}_{\parallel}, \vec{e}_{\perp 1}, \vec{e}_{\perp 2})$  space is given by

$$\mathcal{T} = T_{HV} = \begin{pmatrix} \sqrt{\frac{m_c}{m_{\parallel}}} & 0 & 0 \\ 0 & \sqrt{\frac{m_c}{m_{\perp}}} & 0 \\ 0 & 0 & \sqrt{\frac{m_c}{m_{\perp}}} \end{pmatrix},$$

but the speed of sound  $v_L$  remains unchanged and isotropic.

In this space,  $k^* = \mathcal{T}k$ ,  $\epsilon = \frac{\hbar^2 k^{*2}}{2m}$ ,  $\hbar \frac{dk^*}{dt} = eE^*$ , and the effective mass is given by  $3/m_c = 1/m_{\parallel} + 2/m_{\perp}$ . The change in velocity, in position space, is found by a back transform, incorporating both the mass and momentum transforms, and is given by  $\delta v = \frac{\hbar}{m} \mathcal{T}k^*$ .

After the Herring-Vogt transform is used to find the electric-field induced acceleration, the electrons shed phonons via the same prescription given to the holes. The phonon and electron momentum is found first in the Herring-Vogt space and the back transform  $\mathcal{T}^{-1}$  is applied to return to position space. The only additional concern is correctly back transforming the phonon momentum due to the non-unitarity of the Herring-Vogt transform. To handle this, we maintain the phonon momentum magnitude (ie, conserve energy), but use the back transform  $\mathcal{T}^{-1}$  to find the correct angular distribution.

### D. Time steps

Determining an *efficient* time step size,  $dt$  for charge transport is complicated since the scattering time  $\tau$  varying as the charge carrier accelerates. In this charge transport model it was decided to use sufficiently small  $dt$  such that  $\tau$  is relatively constant at each iteration. The requirement, *sufficiently small*, in practice means that energy is conserved in the transport process and the following is a detailed description of how this requirement is implemented.

By observing the charge Monte Carlo over numerous field strengths and in germanium, it was observed that scattering limits the maximum possible charge momentum magnitude to about

$$k_{max,el} = 28 \times v_L(|\vec{E}|/10)^{1/3}$$

$$k_{max,h} = 14.72 \times v_L(|\vec{E}|/10)^{1/3}$$

for electrons and holes respectively. These momenta  $k$  are then used to determine stepping times which conserve energy; the shed Luke phonon energy must equal the change in potential energy  $e\Delta V$  at the carrier drifts. Again running numerous Monte Carlo it is determined that a stepping time of  $dt = \tau/2$  is sufficiently small to conserve energy. Larger stepping times will result in a deficit of Luke phonons being created.

### E. Select constants for charge Monte Carlo

TABLE II: Physical constants for Si and Ge crystals. The isotropic hole effective mass  $m_h$ , and the anisotropic electron effective masses  $m_{\parallel}$  and  $m_{\perp}$  are  $\parallel$  and  $\perp$ , respectively, to the conduction valley axes, and conductivity effective mass  $3/m_c = 1/m_{\parallel} + 2/m_{\perp}$ . The incident energy per final electron-hole pair is  $\epsilon_{eh}$ ,  $s_L$  the speed of sound, and  $l_0 = \pi\hbar^4\rho/(2m^3\Xi^2)$  is the characteristic range for carrier scattering where  $\Xi_1$  (from [32]) or  $\Xi_{fit}$  (fit to data [36]) is the deformation potential.

	Silicon		Germanium	
	Electrons	Holes	Electrons	Holes
$m_h/m_e$	-	0.5	-	0.35
$m_{\parallel}/m_e$	0.91	-	1.58	-
$m_{\perp}/m_e$	0.19	-	0.081	-
$m_c/m_e$	0.26	-	0.12	-
$v_L$ (km/s)	9.0		5.4	
$\rho$ (g/cm <sup>3</sup> )	2.335		5.323	
$\Xi_1$ (eV)	9.0	5.0	11.0	4.6
$\Xi_{fit}$ (eV)	-	-	11.0	3.4
$l_0$ ( $\mu\text{m}$ )	16.9	7.5	257	108

## VI. ELECTRIC-FIELD LOOKUP

### A. Electric-Field Lookup from Triangulated Mesh

A numerical electric field model is necessary for the charge transport described in Section V. The simplest model is a constant, longitudinally directed field however it may be desirable to include fringing fields and details from the electrode structure. A more accurate model will utilize a triangulated mesh. A 3-d mesh contains nodes, with each mesh node containing an associated electric potential  $V$ . At points other than a mesh node, the potential  $V$  must be interpolated. The

MATLAB programming language offers a few options for this interpolation, the fastest of which, utilizing a barycentric-coordinates linear interpolation via the *TriScatteredInterp* class. The Computational Geometry Algorithms Library (CGAL) is available for C++ [37] though this paper will be presented for a MATLAB implementation. Furthermore, the barycentric transformation involves a linear transformation which implies that the electric field is constant within a triangulation, a property which can be exploited to speed up computation.

MATLAB’s method of looking up the potential, while very convenient, is not efficient considering the number of repeated field queries that occur before the carrier has moved to a location with a differing field. Efficiency can be improved by exploiting that a charge remains within its triangle for numerous iterations and that the field is constant with the triangulation. On the contrary, MATLAB solves for the potential at every iteration in its lookup procedure, which is a bit slow. These repeated searches can be avoided but at the expense of significant code complexity. The effort is justified however as charge transport imposes a dominant computational expense in Monte Carlo.

### B. Barycentric Coordinates

Given a triangulation (the mesh is made of tetrahedra in 3-space but the term triangulation often persists) with four node points  $\mathbf{r}_1, \mathbf{r}_2, \mathbf{r}_3$ , and  $\mathbf{r}_4$ , the arbitrary point  $\mathbf{r}$  can be described by the barycentric coordinates  $\lambda_1, \lambda_2, \lambda_3$ , and  $\lambda_4$  where

$$\mathbf{r} = \lambda_1 \mathbf{r}_1 + \lambda_2 \mathbf{r}_2 + \lambda_3 \mathbf{r}_3 + \lambda_4 \mathbf{r}_4. \quad (8)$$

The additional constraint is imposed that

$$\lambda_1 + \lambda_2 + \lambda_3 + \lambda_4 = 1. \quad (9)$$

The barycentric coordinates  $\lambda$  become more intuitive when thought of as area (volume in 3-d) coordinates (see Figure 9). In this paradigm, consider the 2-d node points  $\mathbf{r}_1, \mathbf{r}_2$ , and  $\mathbf{r}_3$  along with the probe point  $\mathbf{r}$ . To start with, lets normalize the area enclosed by  $\mathbf{r}_1, \mathbf{r}_2$ , and  $\mathbf{r}_3$  to 1 (this normalization is equivalent to the constraint  $\sum_i \lambda_i = 1$ ). Then we can consider the three different areas enclosed by 1)  $\mathbf{r}_2, \mathbf{r}_3$ , and  $\mathbf{r}$  ( $a_1$ ), 2)  $\mathbf{r}_1, \mathbf{r}_3$ , and  $\mathbf{r}$  ( $a_2$ ) and 3)  $\mathbf{r}_1, \mathbf{r}_2$ , and  $\mathbf{r}$  ( $a_3$ ). It turns out that these areas ( $a_1, a_2, a_3$ ) are identically equal to the barycentric coordinates  $\lambda_1, \lambda_2$ , and  $\lambda_3$ , providing a quick and intuitive interpretation of the barycentric coordinates. The process and interpretation is the same in 3-d when volume is substituted for area. It is not actually recommended to calculate  $\lambda$  through this procedure but to instead follow the procedure in Section VI C.

### C. Barycentric Coordinate Formulae

In this section we derive formulae useful for solving the barycentric coordinates and electric-potential. We start again with the definitions given by equations 8 and 9. After separating equation 8 into the  $\mathbf{x}, \mathbf{y}$ , and  $\mathbf{z}$  components we can solve for the  $\lambda$  through the following linear procedures and the formula is written out explicitly below.

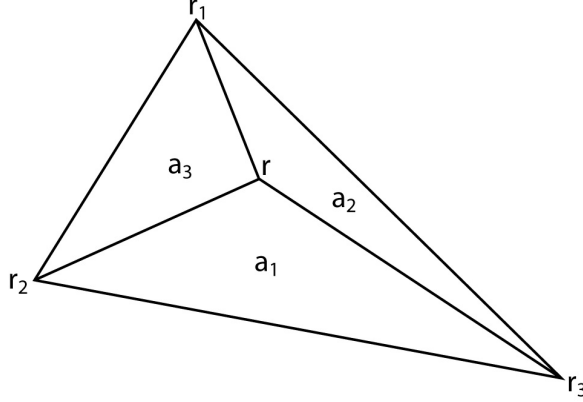


FIG. 9: Mesh node points  $\mathbf{r}_1, \mathbf{r}_2$ , and  $\mathbf{r}_3$  along with the probe point  $\mathbf{r}$ . The areas  $a_1, a_2$  and  $a_3$  are identically equal to the barycentric coordinates  $\lambda_1, \lambda_2$  and  $\lambda_3$ .

$$T = \begin{pmatrix} x_1 - x_4 & x_2 - x_4 & x_3 - x_4 \\ y_1 - y_4 & y_2 - y_4 & y_3 - y_4 \\ z_1 - z_4 & z_2 - z_4 & z_3 - z_4 \end{pmatrix}.$$

$$\begin{pmatrix} \lambda_1 \\ \lambda_2 \\ \lambda_3 \end{pmatrix} = T^{-1}(\mathbf{r} - \mathbf{r}_4) = T^{-1} \begin{pmatrix} x - x_4 \\ y - y_4 \\ z - z_4 \end{pmatrix}, \quad (10)$$

where  $\lambda_4 = 1 - (\lambda_1 + \lambda_2 + \lambda_3)$ . Explicitly we can write out

$$T^{-1} = \frac{1}{\det(T)} \begin{pmatrix} (y_2 - y_4)(z_3 - z_4) - (y_3 - y_4)(z_2 - z_4) \dots \\ (z_2 - z_4)(x_3 - x_4) - (z_3 - z_4)(x_2 - x_4) \dots \\ (x_2 - x_4)(y_3 - y_4) - (x_3 - x_4)(y_2 - y_4) \\ (y_3 - y_4)(z_1 - z_4) - (y_1 - y_4)(z_3 - z_4) \dots \\ (z_3 - z_4)(x_1 - x_4) - (z_1 - z_4)(x_3 - x_4) \dots \\ (x_3 - x_4)(y_1 - y_4) - (x_1 - x_4)(y_3 - y_4) \\ (y_1 - y_4)(z_2 - z_4) - (y_2 - y_4)(z_1 - z_4) \dots \\ (z_1 - z_4)(x_2 - x_4) - (z_2 - z_4)(x_1 - x_4) \dots \\ (x_1 - x_4)(y_2 - y_4) - (x_2 - x_4)(y_1 - y_4) \end{pmatrix}. \quad (11)$$

where  $\det(T) =$

$$\begin{aligned} & (x_1 - x_4) \times [(y_2 - y_4)(z_3 - z_4) - (y_3 - y_4)(z_2 - z_4)] + \dots \\ & (x_2 - x_4) \times [(y_3 - y_4)(z_1 - z_4) - (y_1 - y_4)(z_3 - z_4)] + \dots \\ & (x_3 - x_4) \times [(y_1 - y_4)(z_2 - z_4) - (y_2 - y_4)(z_1 - z_4)]. \end{aligned}$$

The potential is simple to solve for in the barycentric coordinate system and equal to  $V = \lambda_1 V_1 + \lambda_2 V_2 + \lambda_3 V_3 + \lambda_4 V_4$ . This procedure is more obvious when one considers the connection to area coordinates.

#### D. Barycentric Coordinate Procedures and Shortcuts in the DMC

The procedure for finding which tetrahedra a charge resides in is not unique and a canned MATLAB procedure (or CGAL library in C++) can be utilized for this step. After the tetrahedra in which the carrier resides in is determined, the electric field,  $\mathbf{E} = -\nabla V$  is computed. This can be performed by probing the potential at four locations ( $\mathbf{r}$ ,  $\mathbf{r} + \delta\mathbf{x}$ ,  $\mathbf{r} + \delta\mathbf{y}$  and  $\mathbf{r} + \delta\mathbf{z}$ ) and computing gradients. The drawback is that this procedure requires conversion to barycentric coordinates and electric potential lookup for three additional points. These steps can be eliminated with some simple derivations that our outlined below. Most of these steps provide a conceptual framework and only the last step is actually computed.

First we consider two points  $\mathbf{r}'$  and  $\mathbf{r}'' = \mathbf{r}' + \delta\mathbf{x}$  and find their associate barycentric coordinates  $\lambda'$  and  $\lambda''$ .

$$\begin{pmatrix} \lambda'_1 \\ \lambda'_2 \\ \lambda'_3 \end{pmatrix} = T^{-1} \begin{pmatrix} x' - x_4 \\ y' - y_4 \\ z' - z_4 \end{pmatrix}.$$

and

$$\begin{pmatrix} \lambda''_1 \\ \lambda''_2 \\ \lambda''_3 \end{pmatrix} = T^{-1} \begin{pmatrix} x'' - x_4 \\ y'' - y_4 \\ z'' - z_4 \end{pmatrix},$$

where, as always,  $\lambda_4$  is constrained by  $\sum \lambda = 1$ . Next we solve for the potentials  $V'$  and  $V''$

$$V' = \lambda'_1 V_1 + \lambda'_2 V_2 + \lambda'_3 V_3 + \lambda'_4 V_4 = \lambda' \mathbb{V}$$

and

$$V'' = \lambda''_1 V_1 + \lambda''_2 V_2 + \lambda''_3 V_3 + \lambda''_4 V_4 = \lambda'' \mathbb{V},$$

where  $\mathbb{V} = (V_1, V_2, V_3, V_4)$ .

It follows that  $E_x = (V' - V'')/\delta x$  but another route is preferable. We can define  $\delta\lambda_{1,2,3} =$

$$\lambda'_{1,2,3} - \lambda''_{1,2,3} = -T^{-1} \begin{pmatrix} \delta x \\ 0 \\ 0 \end{pmatrix}.$$

The fourth element in  $\delta\lambda$  is determined by remembering that  $\sum \lambda' = \sum \lambda'' = 1$  it follows that  $\sum \delta\lambda = 0$  and therefore  $\delta\lambda_4 = -(\delta\lambda_1 + \delta\lambda_2 + \delta\lambda_3)$ . We can define a matrix related to  $T^{-1}$  but of size  $4 \times 3$  to make future calculations easier,

$$\mathbb{T}^{-1} = \begin{pmatrix} T^{-1}_{1,1} & T^{-1}_{1,2} & T^{-1}_{1,3} \\ T^{-1}_{2,1} & T^{-1}_{2,2} & T^{-1}_{2,3} \\ T^{-1}_{3,1} & T^{-1}_{3,2} & T^{-1}_{3,3} \\ -\sum_i T^{-1}_{i,1} & -\sum_i T^{-1}_{i,2} & -\sum_i T^{-1}_{i,3} \end{pmatrix}. \quad (12)$$

We have now obtained a convenient and efficient method for calculating  $E_x$

$$\begin{aligned} E_x &= \frac{1}{\delta x} \mathbb{V} \delta\lambda = \frac{1}{\delta x} \mathbb{V} \mathbb{T}^{-1} \begin{pmatrix} \delta x \\ 0 \\ 0 \end{pmatrix} = \mathbb{V} \mathbb{T}^{-1} \begin{pmatrix} 1 \\ 0 \\ 0 \end{pmatrix} \\ &= V_1 \mathbb{T}^{-1}_{1,1} + V_2 \mathbb{T}^{-1}_{2,1} + V_3 \mathbb{T}^{-1}_{3,1} + V_4 \mathbb{T}^{-1}_{4,1} \end{aligned} \quad (13)$$

and similarly for  $E_y$  and  $E_z$ . Equations 12 and 13 are used in Monte Carlo and the fields are reused until the charge leaves the triangle boundaries.

### E. Determining if a Charge Leaves a Triangle

The assumption that is exploited in these computations is that the charge remains in a particular triangle for many iterations. This is true, especially in the detector bulk where mesh nodes are sparse, but eventually the charge will enter a different triangle. With the concept of area components, it is clear that one of the barycentric coordinates  $\lambda$  will be zero when the charge is at a surface. By continuation, the same  $\lambda$  will become negative when the charge leaves the triangle. This can be tested efficiently via the linear calculations already derived in Equation 10. When a charge enters a new triangle then  $T$ ,  $\mathbb{T}$  and  $\mathbf{E}$  must be recalculated and stored to memory.

## VII. TRANSITION EDGE SENSOR SIMULATIONS

### A. Introduction

Energy collected in the aluminum fins diffuses through the aluminum fins and is collected into the tungsten Transition Edge Sensors (TESs) [38, 39] with an efficiency of  $\sim 10\%$ . The aluminum quasiparticle fins combined with the tungsten TESs together are referred to as Quasiparticle-trap-assisted Electrothermal-feedback Transition-edge-sensors (QET) [40]. The quasiparticle downconversion process was described previously in Section IV and here we focus on modeling of the TES sensor, which provides the electrical signal which is readout in the experiment. Compared to the phonon simulations, the TES simulations are a bit simpler; most of the electrical and thermal processes that make up the simulation are likely to be more obvious to the reader.

There are, however, tricky numerical issues in solving for the TES voltages. A description of the process follows, and a flowchart (see Figure 10) helps in understanding it. First, the biasing conditions have to be determined. When a TES is run as a phonon sensor (they are also found in many x-ray detectors), the bias voltage is held constant. However, current–voltage (IV) characterization curves are often studied in which the bias current is swept through a range of values. The biasing circuitry and TES resistance  $R = R(T, I)$ , where  $T$  is temperature and  $I$  is current across some physical extent are modeled. The TES electron temperature is affected by three processes: 1) Joule heating warms the TES; 2) Conduction into the substrate cools it; 3) Diffusion through the TES spreads heat. It is of course the goal to run the simulation both quickly and accurately.

## B. Electrical Circuit Modeling

The TESs are relatively simple to model as each can be thought of as a one dimensional object (see Figure 13). Generally, a TES is modeled with a minimum of two nodes and as many as  $\sim 100$  if it is desired to reproduce superconducting-normal phase separation [41, 42]. The functional form of the resistance at each node has generally been given by

$$R_{i,j} = \frac{R_{max} - R_{min}}{2} \left\{ 1 + \tanh \left[ \frac{T_{i,j} - T_c \left( 1 - \frac{|I_{i,j}|}{I_c} \right)^{n_{sc}}}{T_w} \right] \right\},$$

for  $I_{i,j}$  small and  $R_{i,j} = R_{max}$ , for  $I_{i,j}$  large; where  $R_{max}$  is the TES's resistance in the normal state,  $R_{min}$  is the superconducting resistance (numerically it is best to not set  $R_{min}$  to zero but rather some small value  $\sim 10^{-8} \Omega$ ),  $T_c$  is the midpoint temperature of the superconducting transition,  $T_w$  is the temperature width of the superconducting transition,  $I_c$  is the critical current (see below), and  $n_{sc} \sim 2/3$  is motivated by [43, 44].

The critical current is provided by Ginzburg-Landau theory and near  $T_c$  is equal to  $I_c = 3.52 \sqrt{\frac{k_B C_n}{\hbar R_n}} T_c \left( 1 - \frac{T}{T_c} \right)^{3/2}$ , where  $k_B$  is the Boltzmann constant, and  $C_n$  is the heat capacity. Special care needs to be taken when calculating the critical current when modeling TESs that are wired in parallel. Implicit in the Ginzburg-Landau equation is that *one* thin film superconductor contains the current while in CDMS detectors, the TES is distributed over  $n_{TES}$  TESs. This cause the heat capacity  $C_n$  to scale down by  $1/n_{TES}$  and  $I_c$  scales down by  $1/\sqrt{n_{TES}}$  for each of the TESs. There is an offsetting factor when the currents from all the  $n_{TES}$  TES which causes  $I_c$  to scale up by  $n_{TES}$ . The end result is that  $I_c$  for the entire collection of  $n_{TES}$  parallel TESs scales like  $\sqrt{n_{TES}}$ .

The requirement that the resistance  $R = R_{max}$  at large current  $I$  is required for IV curves that sweep from the superconducting to normal states. There is no precise definition of large  $I$ , but it is chosen to be much higher than the quiescent operating current while low enough that it is not too much higher than the normal to superconducting transition current. A plot of  $R = R(T, I)$ ,  $\alpha = dR/dT \times T/R$  and  $\beta = dR/dI \times I/R$  is shown in Figure 11 .

Modeling of the TES and biasing circuitry (see Figure 12) is complicated by our desire to be able to create IV curves in which the bias voltage ( $V_{bias}$ ) is swept from zero to some large value and back to zero again. This difficulty comes about from the current dependence on resistance and also due to the sharp change in current that occurs during the transition from the superconducting to ohmic states. This difficulty can be overcome if we use a damping factor to not allow the resistance

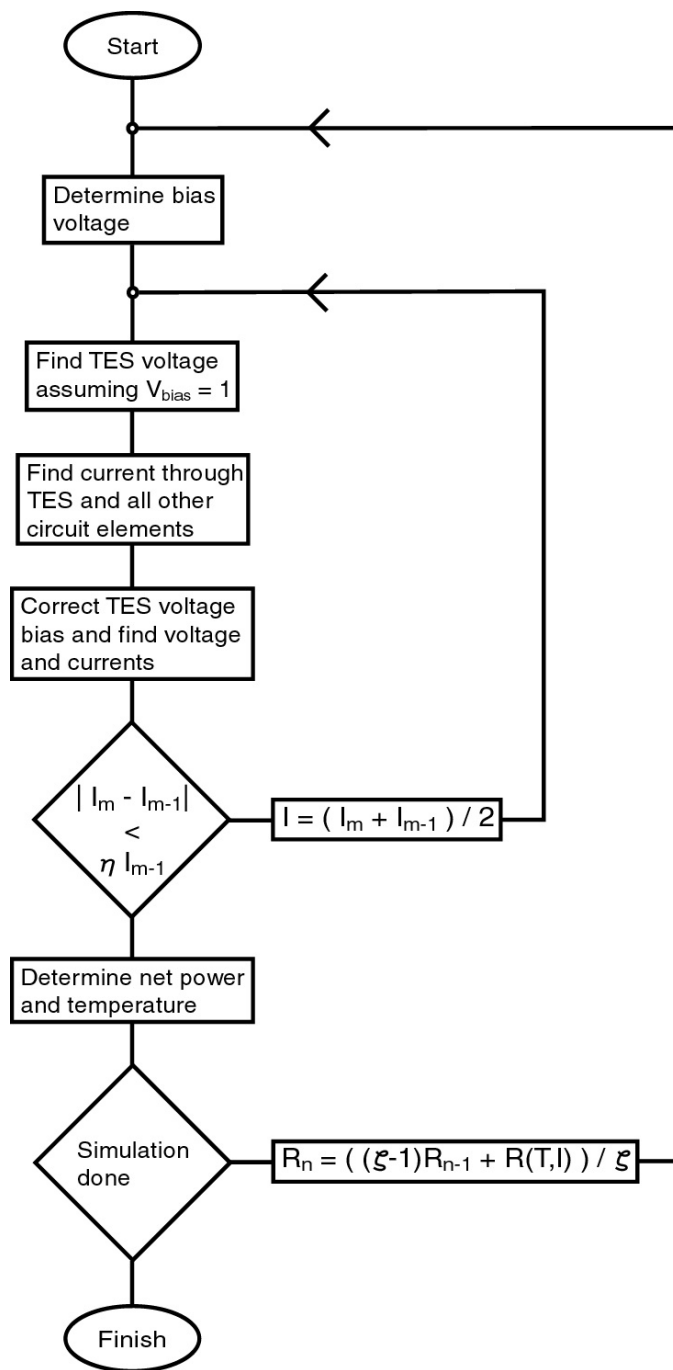


FIG. 10: TES simulation flowchart.

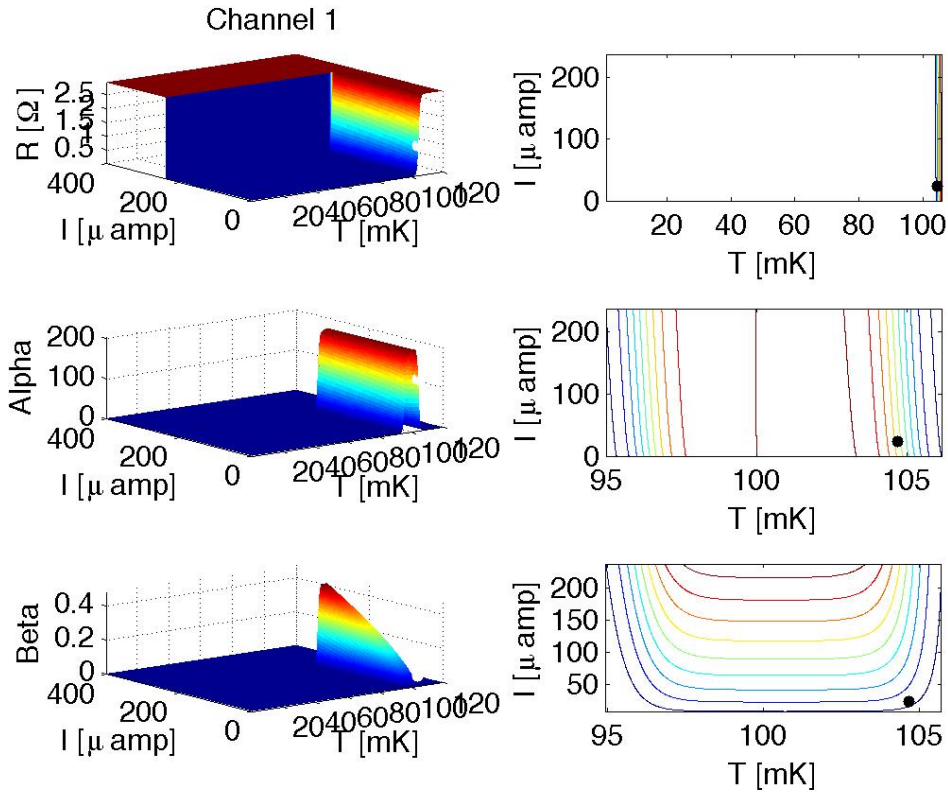


FIG. 11: Surface and contour plots of  $R = R(T, I)$ ,  $\alpha = \alpha(T, I)$  and  $\beta = \beta(R, I)$  for a high- $T_c$ , inner iZip channel.

to change too rapidly. To determine the TES resistance at step  $n$  we let

$$R_n = \frac{(\zeta - 1)R_{n-1} + R(T, I)}{\zeta}$$

where  $\zeta$  is a stabilization constant whose value  $\sim 5$  is found by trial and error. Picking a large value makes current transitions numerically stable, but requires slower step sizes  $dt$  to retain accuracy.

Next, we solve for the voltages at each TES node (to be discussed below) and determine the resulting voltages and currents. We also model the inductor as discussed below. It is likely that the currents that we solve for differ from those that we originally used to compute  $R = R(T, I)$ . I keep evaluating  $R_m(T, I_m)$ ,  $V$  and  $I$  letting

$$I_m = \frac{I_{m-1} + I_{m-2}}{2}$$

until

$$|I_m - I_{m-1}| < \eta I_{m-1}$$

where  $\eta \sim 10^{-3}$  is satisfied for all nodes, ensuring a self consistent answer. I have enumerated the individual steps  $m$  here to prevent confusing them with the steps  $n$  that involve simulation time steps  $dt$  (again, see Figure 10).

The rest of the circuit, including the inductor, is modeled by finding the macroscopic current through the TES  $I_n$ . A simple circuit analysis reveals that it is given by

$$I_n = \frac{\frac{V_{bias}R_{shunt}}{R_{bias}+R_{shunt}} + \frac{LI_{n-1}}{dt}}{\frac{R_{bias}R_{shunt}}{R_{bias}+R_{shunt}} + R_{true} + R_{parasitic} + \frac{L}{dt}}.$$

### 1. TES Voltage Modeling

In the simulation, temperature, and therefore resistance, is modeled at each node. However for the purpose of modeling the electrical circuit the interconnects need to have a resistance which is given by averaging the resistance of the two nodes that they connect.

We will now set up the system of equations  $\mathbf{G}V = B$  where the conductance matrix,  $\mathbf{G}$ , is a sparse, square matrix and  $B$  is a vector that described the electrical boundary conditions. The form of the conductance matrix  $\mathbf{G}$  is simplified significantly if we treat the individual TESs as one dimensional object. In general (regardless of the 1-d simplification) nodes either are voltage biased (which includes grounding) or are not. Those that are not biased (or grounded) impose current conservation requirements. From Kirchhoff's current law, the equation to be satisfied for nodes that have four adjacent nodes is

$$\frac{V_{left} - V}{R_{left}} + \frac{V_{right} - V}{R_{right}} = 0.$$

Nodes without four adjacent nodes will result in the appropriate terms being removed, for example a node with a top, left and right neighbors is given by

$$\frac{V_{left} - V}{R_{left}} + \frac{V_{right} - V}{R_{right}} = 0.$$

The result on the  $\mathbf{G}$  matrix is straightforward. The diagonal elements are given by

$$\mathbf{G}_{ii} = -\frac{1}{R_{left}} - \frac{1}{R_{right}}.$$

The non-diagonal elements that couple adjacent nodes are given by

$$\mathbf{G}_{terms \text{ which couple adjacent nodes}} = \frac{1}{R_{adjacent}}.$$

Nodes that have their voltage fixed either through voltage biasing or grounding satisfy the equation  $V = V_{bias}$ . They are given the coupling terms

$$\mathbf{G}_{ii} = 1,$$

the other terms in the row are

$$\mathbf{G}_{ij} = 0,$$

where  $i \neq j$ .

Now we can set up  $B$  and complete Kirchoff's current law. For the rows in  $\mathbf{G}$  that describe current conservation,

$$B_i = 0.$$

Whereas the rows in  $\mathbf{G}$  that describe voltage biasing,

$$B_i = V_{bias}.$$

We can then solve

$$V = \mathbf{G}^{-1}B,$$

to find the voltages at all TES nodes.

### C. Thermal Processes

After determining the voltages at each node, Joule heating is calculated by

$$P_J = \frac{V^2}{R}.$$

Power into the substrate is given by

$$P_S = -\Sigma (T_{TES}^n - T_{substrate}^n).$$

Thermal diffusion is simplified by assuming that the QETs are thermally decoupled from each other due to poor conduction through the substrate. The process is then described by a 1-d diffusion process

$$\frac{\partial T}{\partial t} = D\Delta T,$$

where

$$\Delta T = \nabla \cdot \nabla T = \frac{\partial^2 T}{\partial x^2}$$

and  $D$  is given by  $K/C_V$  where  $K$  is the thermal conductivity and  $C_V$  is the heat capacity per unit volume [13].

For non-boundary nodes,  $\Delta T$  can be approximated by considering the midpoint and two adjoining points. To see this let us first consider just one dimension, specifically the term  $\frac{\partial^2 T}{\partial x^2}$ . First we compute  $\frac{\partial T}{\partial x}$ . In the discrete approximation we can consider some point  $T_i$  and either its right neighbor or left neighbor  $T_{i+1}$  or  $T_{i-1}$ , where  $i$  represents the position of some node in the  $x$  direction. We obtain either

$$\left. \frac{\partial T}{\partial x} \right|_{right} \rightarrow \frac{T_{i+1} - T_i}{\delta x}$$

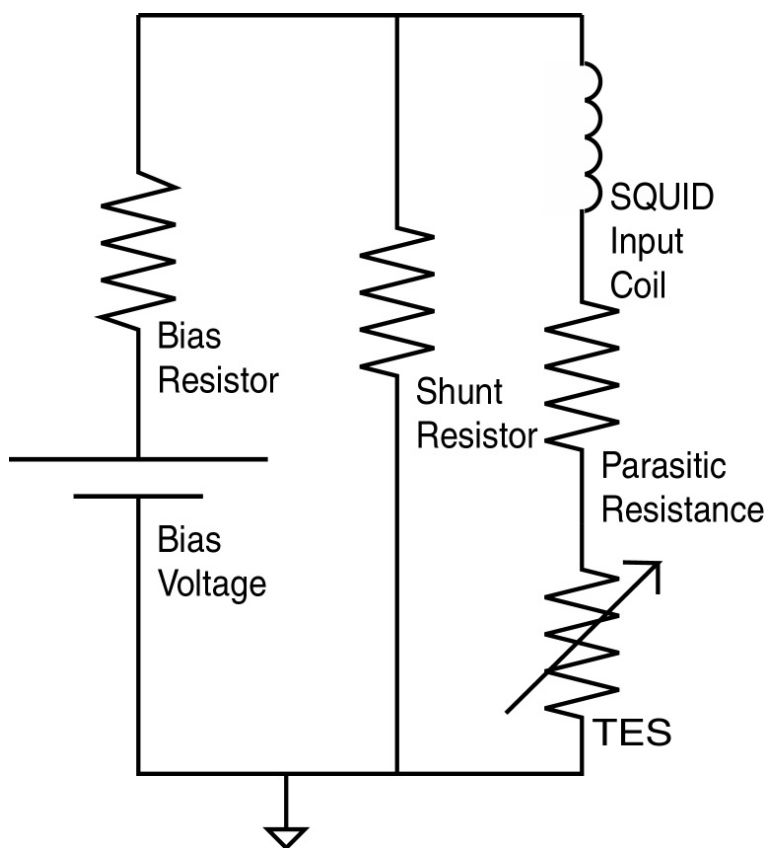


FIG. 12: TES simulation biasing circuitry. Modeling reflects the biasing circuitry.

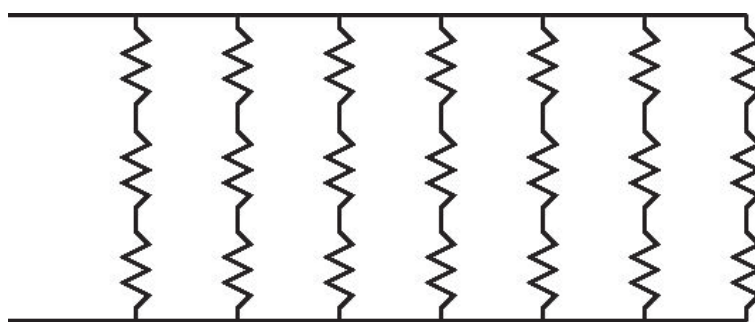


FIG. 13: TES resistor interconnects as modeled using a finite element approximation.

or

$$\frac{\partial T}{\partial x} \Big|_{left} \rightarrow \frac{T_i - T_{i-1}}{\delta x},$$

where  $\rightarrow$  denotes the move from continuous to discrete space. Next we compute

$$\begin{aligned} \frac{\partial}{\partial x} \frac{\partial T}{\partial x} &\rightarrow \frac{\frac{\partial T}{\partial x} \Big|_{right} - \frac{\partial T}{\partial x} \Big|_{left}}{\delta x} \\ &= \frac{T_{i-1} - 2T_i + T_{i+1}}{(\delta x)^2}. \end{aligned} \quad (14)$$

Boundary nodes are computed differently. To conserve energy we impose the Neumann boundary condition

$$\nabla T|_{boundary} = 0.$$

Making the discrete approximation is simple, we compute

$$T_i - T_{i-1} = 0 \quad (15)$$

for boundary nodes.

$T$  will be the temperature matrix of size  $n \times m$  where  $n$  and  $m$  represents the nodes in the  $y$  and  $x$  directions respectively. It would be nice to convert the following procedures for computing  $\Delta T$  into a matrix operation which considering Equations 14 and 15 is fortunately is quite simple. The matrix  $\tilde{\Delta}_x$  is of size  $m \times m$  and allows discrete calculations of  $\Delta T$ . Specifically,

$$\frac{\partial^2 T}{\partial x^2} \rightarrow \frac{T \tilde{\Delta}_x}{(\delta x)^2}$$

where  $\tilde{\Delta}_x$  has the form

$$\begin{pmatrix} -1 & 1 & 0 & 0 & \cdots & 0 & 0 & 0 \\ 1 & -2 & 1 & 0 & \cdots & 0 & 0 & 0 \\ 0 & 1 & -2 & 1 & \cdots & 0 & 0 & 0 \\ & & & & \ddots & & & \\ 0 & 0 & 0 & 0 & \cdots & 1 & -2 & 1 \\ 0 & 0 & 0 & 0 & \cdots & 0 & 1 & -1 \end{pmatrix}. \quad (16)$$

This form is equivalent to Equations 14 and 15 and that the signs are correct for the boundary nodes to ensure heat moves from hot to cold nodes.

The diffusion algorithm is then given by

$$T_{n+1} = T_n + D \delta t \left( \frac{T \tilde{\Delta}_x}{(\delta x)^2} \right).$$

The algorithm should be stable as long as the Courant–Friedrichs–Lewy condition

$$\delta t < \frac{(\delta x)^2}{2D}$$

is satisfied [45, 46] but the Joule heating and substrate cooling terms result in a less stable algorithm and the stability is observed to become poorer as the TES cell size is reduced. The onset of instability is due to local temperature deviations due to small numerical imprecision. These deviations can be recognized by comparing the maximum absolute temperature difference in adjacent cells  $T_{diff,adj} = \max(|(T_{i+1} - T_i)|)$  to the maximal temperature difference in the TES  $T_{diff,max} = \max(T) - \min(T)$ . The number of time steps is then scaled up by  $T_{diff,adj}/T_{diff,max} \times N/f$ , where  $N$  is the number of cells along the TES and  $f$  is a fudge factor  $\sim 10$ .

#### D. Parsing Phonons Into The TESs

One issue that needs to be considered before running a TES simulator is the parsing of phonons into the multiple QETs which are wired in parallel. It is generally more computationally efficient to ignore the exact location with and without aluminum coverage and to use an average approximation. In this case, we need only determine the physical region of each QET structure. This can be approximated by assuming each QET to have the same area. For a TES channel with radial and angular extent  $R_1$ ,  $R_2$ ,  $\Theta_1$  and  $\Theta_2$  and containing  $N$  discrete circuit elements, the area of each element is simply

$$a = \frac{1}{2N} (R_2^2 - R_1^2) (\Theta_2 - \Theta_1). \quad (17)$$

For the first ring of TES elements we could also consider the area of each element to be

$$a = \frac{1}{2} \delta\theta [(R_1 + \delta r)^2 - R_1^2] = \frac{\delta\theta}{2} (2R_1\delta r + \delta r^2), \quad (18)$$

where  $\delta r$  and  $\delta\theta$  are the elements' size in the radial and angular directions. Equating the two descriptions of area we get

$$\frac{1}{2N} (R_2^2 - R_1^2) (\Theta_2 - \Theta_1) = \delta\theta \left( R_1\delta r + \frac{1}{2}\delta r^2 \right). \quad (19)$$

We can now impose a proportionality between the element's linear dimensions in the radial and theta direction (measured at  $r = R_1 + \delta r/2$ ) then we get the relationship  $\delta r = c(R_1 + \delta r/2)\delta\theta$ , where  $c$  is a proportionality constant. This can be substituted into Equation 19 to eliminate  $\delta\theta$  and we obtain

$$N \delta r^3 + 2R_1N \delta r^2 - \frac{2c}{4} (R_2^2 - R_1^2) (\Theta_2 - \Theta_1) \delta r - \frac{2c}{2} (R_2^2 - R_1^2) (\Theta_2 - \Theta_1) R_1 = 0. \quad (20)$$

This equation can be solved for  $\delta r$  and provides one real root.

If  $\delta r > R_2 - R_1$  then the lower value  $R_2 - R_1$  is of course selected otherwise a  $\delta r$  for each ring is proposed to be equal and rounded off to  $(R_2 - R_1)/\text{round}((R_2 - R_1)/\delta r)$ . The round is included to ensure an integer number of rings. The number of  $\theta$  divisions  $n$  for this ring is simply

$$n = \text{round}((R_1 + \delta r)^2 - R_1^2 (\Theta_2 - \Theta_1) / 2/a), \quad (21)$$

where the number of elements is further constrained by  $n \geq 1$ .

This solution isn't really self consistent since we have imposed too many competing desires, namely that the radial and angular dimensions satisfy a proportionality condition and that there are an integer number of elements in a ring. The former can be relaxed, but the integer number of elements is mandatory. We can obtain a solution with dimensions close to the desired proportionality condition if we set  $\delta\theta = (\Theta_2 - \Theta_1)/n$  and  $\delta r = \sqrt{2a/\delta\theta + R_1^2} - R_1$ . After this first ring is built up the procedure repeats, with  $R_1 \rightarrow R_1 - \delta r$  until the entire channel area has been segmented.

### VIII. FINAL REMARKS

This paper has covered many physics and Monte Carlo topics in cryogenic radiation-detectors that utilize phonon and ionization readout. The bulk response is different for gamma and neutron interactions, the former producing a larger ratio of ionization energy. Propagation of both the phonons and charge carriers is anisotropic, the phonons transport dependent on dispersion relations and the charge carrier transport dependent on mass tensors. Phonon interactions are complicated at the surface by electron-phonon downconversion requiring additional Monte Carlo effort. The TES readout simulation is relatively straightforward relying on basic thermal and electrical processes. Various numerical techniques including PDF sampling and tricks for improving efficiency have been discussed.

Monte Carlo of detectors is a valuable tool for detector design, characterization and data analysis. Often counter intuitive results can be quickly discovered in Monte Carlo which aids in prioritizing laboratory R&D efforts. Furthermore, Monte Carlo can help to explain features in data, or at least rule out models.

Detailed Monte Carlo studies in CDMS [42, 47–52] and EDELWEISS [53, 54] detectors can be found in the literature.

With the power of Monte Carlo and increased use of low temperature cryogenic detectors, a general package is becoming more appealing. The GEANT4 collaboration is beginning to implement phonon and charge transport modules into the GEANT4 toolkit and will expand the benefits of this research to others outside the cryogenic detector community [55].

### Acknowledgments

We would like to thank numerous CDMS collaborators for valuable discussions over the years especially Paul Brink, Blas Cabrera, Enectali Figueroa-Feliciano, Matt Pyle, Bernard Sadoulet, Kyle Sundqvist and Betty Young. The author also acknowledges that BC generously provided his note on “Electron-Phonon Scattering”, which was adapted for this review. Kevin McCarthy has been an invaluable contributor to the CDMS Monte Carlo studies cited in the references.

- 
- [1] CDMS II Collaboration and Ahmed, Z. and Akerib, D. S. and Arrenberg, S. and Bailey, C. N. and Balakishiyeva, D. and Baudis, L. and Bauer, D. A. and Brink, P. L. and Bruch, T. and Bunker, R. and Cabrera, B. and Caldwell, D. O. and Cooley, J. and Cushman, P. and Daal, M. and DeJongh, F. and Dragowsky, M. R. and Duong, L. and Fallows, S. and Figueroa-Feliciano, E. and Filippini, J. and Fritts, M. and Golwala, S. R. and Grant, D. R. and Hall, J. and Hennings-Yeomans, R. and Hertel, S. A. and Holmgren, D. and Hsu, L. and Huber, M. E. and Kamaev, O. and Kiveni, M. and Kos, M. and Leman, S. W. and Mahapatra, R. and Mandic, V. and McCarthy, K. A. and Mirabolfathi, N. and Moore, D. and Nelson, H. and Ogburn, R. W. and Phipps, A. and Pyle, M. and Qiu, X. and Ramberg, E. and Rau, W. and Reisetter, A. and Saab, T. and Sadoulet, B. and Sander, J. and Schnee, R. W. and Seitz, D. N. and Serfass, B. and Sundqvist, K. M. and Tarka, M. and Wikus, P. and Yellin, S. and Yoo, J. and Young, B. A. and Zhang, J. , “Dark Matter Search Results from the CDMS II Experiment,” *Science* **327**, 2010.
- [2] Ahmed, Z. and Akerib, D. S. and Arrenberg, S. and Bailey, C. N. and Balakishiyeva, D. and Baudis, L. and Bauer, D. A. and Brink, P. L. and Bruch, T. and Bunker, R. and Cabrera, B. and Caldwell, D. O. and Cooley, J. and Do Couto E Silva, E. and Cushman, P. and Daal, M. and DeJongh, F. and

- di Stefano, P. and Dragowsky, M. R. and Duong, L. and Fallows, S. and Figueroa-Feliciano, E. and Filippini, J. and Fox, J. and Fritts, M. and Golwala, S. R. and Hall, J. and Hennings-Yeomans, R. and Hertel, S. A. and Holmgren, D. and Hsu, L. and Huber, M. E. and Kamaev, O. and Kiveni, M. and Kos, M. and Leman, S. W. and Liu, S. and Mahapatra, R. and Mandic, V. and McCarthy, K. A. and Mirabolfathi, N. and Moore, D. and Nelson, H. and Ogburn, R. W. and Phipps, A. and Pyle, M. and Qiu, X. and Ramberg, E. and Rau, W. and Reisetter, A. and Resch, R. and Saab, T. and Sadoulet, B. and Sander, J. and Schnee, R. W. and Seitz, D. N. and Serfass, B. and Sundqvist, K. M. and Tarka, M. and Wikus, P. and Yellin, S. and Yoo, J. and Young, B. A. and Zhang, J., “Results from a Low-Energy Analysis of the CDMS II Germanium Data,” *Physical Review Letters* **106**, 2011.
- [3] E. Armengaud and C. Augier and A. Benoit and L. Berge and O. Besida and J. Blumer and A. Broniatowski and A. Chantelauze and M. Chapellier and G. Chardin and F. Charlieux and S. Collin and X. Defay and M. De Jesus and P. Di Stefano and Y. Dolgorouki and J. Domange and L. Dumoulin and K. Eitel and J. Gascon and G. Gerbier and M. Gros and M. Hannawald and S. Herve and A. Juillard and H. Kluck and V. Kozlov and R. Lemrani and P. Loaiza and A. Lubashevskiy and S. Marnieros and X.-F. Navick and E. Olivieri and P. Pari and B. Paul and S. Rozov and V. Sanglard and S. Scorza and S. Semikh and A.S. Torrento-Coello and L. Vagneron and M.-A. Verdier and E. Yakushev, “First results of the EDELWEISS-II WIMP search using Ge cryogenic detectors with interleaved electrodes,” *Physics Letters B* **687**, 2010.
- [4] Geant4 Collaboration and Agostinelli, S. and Allison, J. and Amako, K. and Apostolakis, J. and Araujo, H. and Arce, P. and Asai, M. and Axen, D. and Banerjee, S. and Barrand, G. and Behner, F. and Bellagamba, L. and Boudreau, J. and Broglia, L. and Brunengo, A. and Burkhardt, H. and Chauvie, S. and Chuma, J. and Chytracek, R. and Cooperman, G. and Cosmo, G. and Degtyarenko, P. and dell’Acqua, A. and Depaola, G. and Dietrich, D. and Enami, R. and Feliciello, A. and Ferguson, C. and Fesefeldt, H. and Folger, G. and Foppiano, F. and Forti, A. and Garelli, S. and Giani, S. and Giannitrapani, R. and Gibin, D. and Gómez Cadenas, J. J. and González, I. and Gracia Abril, G. and Greeniaus, G. and Greiner, W. and Grichine, V. and Grossheim, A. and Guatelli, S. and Gumplinger, P. and Hamatsu, R. and Hashimoto, K. and Hasui, H. and Heikkinen, A. and Howard, A. and Ivanchenko, V. and Johnson, A. and Jones, F. W. and Kallenbach, J. and Kanaya, N. and Kawabata, M. and Kawabata, Y. and Kawaguti, M. and Kelner, S. and Kent, P. and Kimura, A. and Kodama, T. and Kokoulin, R. and Kossov, M. and Kurashige, H. and Lamanna, E. and Lampén, T. and Lara, V. and Lefebvre, V. and Lei, F. and Liendl, M. and Lockman, W. and Longo, F. and Magni, S. and Maire, M. and Medernach, E. and Minamimoto, K. and Mora de Freitas, P. and Morita, Y. and Murakami, K. and Nagamatu, M. and Nartallo, R. and Nieminen, P. and Nishimura, T. and Ohtsubo, K. and Okamura, M. and O’Neale, S. and Oohata, Y. and Paech, K. and Perl, J. and Pfeiffer, A. and Pia, M. G. and Ranjard, F. and Rybin, A. and Sadilov, S. and di Salvo, E. and Santin, G. and Sasaki, T. and Savvas, N. and Sawada, Y. and Scherer, S. and Sei, S. and Sirotenko, V. and Smith, D. and Starkov, N. and Stoecker, H. and Sulkimo, J. and Takahata, M. and Tanaka, S. and Tcherniaev, E. and Safai Tehrani, E. and Tropeano, M. and Truscott, P. and Uno, H. and Urban, L. and Urban, P. and Verderi, M. and Walkden, A. and Wander, W. and Weber, H. and Wellisch, J. P. and Wenaus, T. and Williams, D. C. and Wright, D. and Yamada, T. and Yoshida, H. and Zschesche, D., “Geant4—a simulation toolkit,” *Nuclear Instruments and Methods in Physics Research A* **506**, 2003.
- [5] G. F. Knoll, *Radiation Detection and Measurement*, John Wiley and Sons, 1989.
- [6] K. Nakamura et al. (Particle Data Group), “The review of particle physics,” *Journal of Physics G* **37**, 2010.
- [7] B. Cabrera, B. L. Dougherty, A. T. Lee, M. J. Penn, J. G. Pronko, and B. A. Young, “Prompt phonon signals from particle interactions in si crystals,” *Journal of Low Temperature Physics* **93**(3-4), pp. 365–375, 1993.
- [8] U. Fano, “Ionization Yield of Radiations. II. The Fluctuations of the Number of Ions,” *Physical Review* **72**, pp. 26–29, July 1947.
- [9] E. Rutherford, “The scattering of  $\alpha$  and  $\beta$  particles by matter and the structure of the atom,” *Philos. Mag.* **6**, p. 21, 1911.
- [10] E. Bonderup, “Penetration of charged particles through matter,” *Lectures notes, Aarhus* , 1978.
- [11] J. Lindhard and V. Nielsen and M. Scharff and P.V. Thomsen, “Integral equations governing radia-

- tion effects (notes on atomic collisions, iii),” *Matematisk-fysiske Meddelelser udgivet af Det Kongelige Danske Videnskabernes Selskab* **33**(10), 1963.
- [12] J. Lewin and P. Smith, “Review of mathematics, numerical factors, and corrections for dark matter experiments based on elastic nuclear recoil,” *Astroparticle Physics* **6**, pp. 87–112, 1996.
  - [13] C. Kittel and H. Kroemer, *Thermal Physics*, W.H. Freeman and Company, 1980.
  - [14] N. W. Ashcroft and N. D. Mermin, *Solid State Physics*, Harcourt Collee Publishers, 1976.
  - [15] J. P. Wolfe, *Imaging Phonons: Acoustic Wave Propagation in Solids*, Cambridge University Press, 1998.
  - [16] G. A. Northrop and J. P. Wolfe, “Ballistic phonon imaging in germanium,” *Physical Review B* **22**, pp. 6196–6212, Dec. 1980.
  - [17] S. Tamura, J. A. Shields, and J. P. Wolfe, “Lattice dynamics and elastic phonon scattering in silicon,” *Physical Review B* **44**, pp. 3001–3011, Aug. 1991.
  - [18] H. J. Maris and S. Tamura, “Anharmonic decay an the propagation of phonons in an isotropically pure crystal at low temperatures: Application to dark-matter detection,” *Physical Review B* **47**, pp. 727–739, Jan. 1993.
  - [19] S. Tamura, “Monte Calro Calculations of Quasidiffusion in Silicon,” *Journal of Low Temperature Physics* **93**(3), pp. 433–438, 1993.
  - [20] J. Maris, “Phonon propagation with isotope scattering and spontaneous anharmonic decay,” *Physical Review B* **41**, pp. 9736–9743, May 1990.
  - [21] M. Msall, S. Tamura, S. Esipov, and J. Wolfe, “Quasidiffusion and the Localized Phonon Source in Photoexcited Si,” *Physical Review Letters* **70**, pp. 3463–3466, May 1993.
  - [22] S. Tamura, “Quasidiffusive propagation of phonons in silicon: Monte Carlo calculations,” *Physical Review B* **48**, pp. 13502–13507, Nov. 1993.
  - [23] W. H. Press, S. A. Teukolsky, W. T. Vetterling, and B. P. Flannery, *Numerical Recipes in C: The Art of Scientific Computing, Second Edition*, Cambridge University Press, 1992.
  - [24] Shin-ichiro Tamura, “Spontaneous decay rates of ta phonons,” *Physical Review B* **31**(4), 1985.
  - [25] Shin-ichiro Tamura, “Spontaneous decay rates of la phonons in quasi-isotropic solids,” *Physical Review B* **31**(4), 1985.
  - [26] Private correspondence between Blas Cabrera and Shin-ichiro Tamura.
  - [27] R. H. Pehl, F. S. Goulding, D. A. Landis, and M. Lenzling, “Accurate determination of the ionization energy in semiconductor detectors,” *Nuclear Instruments and Methods* **59**(1), pp. 45–55, 1968.
  - [28] S.B. Kaplan and C.C. Chi and D.N. Langenber and J.J. Chang and S. Jafarey and D.J. Scalapino, “Quasiparticle and phonon lifetimes in superconductors,” *Physical Review B* **14**(11), p. 4854, 1976.
  - [29] M. Kurakado, “Possibility of high resolution detectors using superconducting tunnel junctions,” *Nuclear Instruments and Methods* **196**, pp. 275–277, 1982.
  - [30] P. L. Brink, *Non-Equilibrium Superconductivity induced by X-ray Photons*. PhD thesis, Oxford University, 1995.
  - [31] W. Sasaki and M. Shibuya and K. Mizuguchi , “Anisotropy of hot electrons in n-type germanium,” *Journal of the Physical Society of Japan* **13**, p. 456, 1958.
  - [32] C. Jacoboni and L. Reggiani, “The monte carlo method for the solution of charge transport in semiconductors with applications to covalent materials,” *Rev. Mod. Phys.* **55**, pp. 645–705, Jul 1983.
  - [33] B. Neganov and V. Trofimov *USSR Patent No 1037771, Otkrytia i izobreteniya* **146**, p. 215, 1985.
  - [34] P. Luke, “Voltage–assisted calorimetric ionization detector,” *Journal of Applied Physics* **64**, p. 6858, 1988.
  - [35] C. Herring and E. Vogt, “Transport and Deformation-Potential Theory for Many-Valley Semiconductors with Anisotropic Scattering,” *Physical Review* **101**(3), p. 944, 1956.
  - [36] K.M. Sundqvist and A. T. J. Phipps and C. N. Bailey and P. L. Brink and B. Cabrera and M. Daal and A. C. Y. Lam and N. Mirabolfathi and L. Novak and M. Pyle and B. Sadoulet and B. Serfass and D. Seitz and A. Tomada and J. J. Yen, “A measurement of electron and hole drift velocities in a germanium <100> cdms detector, at a temperature of 31 millikelvin,” *AIP Conference Series* **1185**, pp. 128–131, 2009.
  - [37] [www.cgal.org](http://www.cgal.org).
  - [38] K. D. Irwin, “An application of electrothermal feedback for high resolution cryogenic particle detec-

- tion,” *Applied Physics Letters* **66**(15), 1995.
- [39] Irwin, K.D. and Hilton, G.C., “Transition-Edge Sensors,” in *Cryogenic Particle Detection*, Enss, Christian, ed., *Topics in Applied Physics* **99**, pp. 81–97, Springer Berlin / Heidelberg, 2005.
- [40] B. Cabrera, “Design considerations for tes and qet sensors,” *Nuclear Instruments & Methods in Physics Research, Section A* **444**(1-2), 2000.
- [41] S. W. Leman, *Development of Phonon-Mediate Transition-Edge-Sensor X-ray Detectors for use in Astronomy*. PhD thesis, Stanford University, 2001.
- [42] A.J. Anderson and S.W. Leman and M. Pyle and E. Figueroa-Feliciano and K. McCarthy and T. Doughty for the SuperCDMS Collaboration, “Simulations of noise in phase-separated transition-edge sensors for supercdms,” *Journal of Low Temperature Physics*, submitted 2011.
- [43] M. Tinkham, *Introduction to Superconductivity*, Krieger Publishing Company, 1975. see page 117.
- [44] K. Irwin, G.C.Hilton, D.A.Wollman, and J. M. Martinis, “Thermal-response time of superconducting transition-edge microcalorimeters,” *Journal of Applied Physics* **83**(8), 1998.
- [45] R. Courant, K. Friedrichs, and H. Lewy, “Über die partiellen Differenzgleichungen der mathematischen Physik,” *Mathematische Annalen* **100**, pp. 32–74, 1928.
- [46] R. L. Burden and J. D. Faires, *Numerical Analysis*, Brooks / Cole Publishing Company, 1997.
- [47] S. Leman, B. Cabrera, K. McCarthy, M. Pyle, R. Resch, B. Sadoulet, K. Sundqvist, P. Brink, M. Cherry, Do Couto E Silva, E., E. Figueroa-Feliciano, N. Mirabolfathi, B. Serfass, and A. Tomada, “Phonon quasidiffusion in cdms large germanium detectors,” *Chinese Journal of Physics (PHONONS 2010 conference proceedings)* **49**, p. 349, 2011.
- [48] S.W. Leman, S. Hertel, P. Kim, B. Cabrera, E. Do Couto E Silva, E. Figueroa-Feliciano, K. McCarthy, R. Resch, B. Sadoulet, K. Sundqvist, and on behalf of the Cryogenic Dark Matter Search collaboration, “Comparison of cdms [100] and [111] oriented germanium detectors,” *Journal of Low Temperature Physics*, submitted 2011.
- [49] S.W. Leman, D. Brandt, P. Brink, B. Cabrera, H. Chagani, M. Cherry, P. Cushman, E. Do Couto E Silva, T. Doughty, E. Figueroa-Feliciano, V. Mandic, K. McCarthy, N. Mirabolfathi, M. Pyle, A. Reisetter, R. Resch, B. Sadoulet, B. Serfass, K. Sundqvist, A. Tomada, B. Young, J. Zhang, and on behalf of the Cryogenic Dark Matter Search collaboration, “Time evolution of electric fields in cdms detectors,” *Journal of Low Temperature Physics*, submitted 2011.
- [50] S.W. Leman, K. McCarthy, P. Brink, B. Cabrera, M. Cherry, E. Do Couto E Silva, E. Figueroa-Feliciano, P. Kim, N. Mirabolfathi, M. Pyle, R. Resch, B. Sadoulet, B. Serfass, K. Sundqvist, , A. Tomada, , and B. Young, “Monte carlo comparisons to a cryogenic dark matter search detector with low transition-edge-sensor transition temperature,” *Review of Scientific Instruments*, submitted 2011.
- [51] K.A. McCarthy and S. W. Leman and A. Anderson and D. Brandt and P.L. Brink and B. Cabrera and M. Cherry and E. Do Couto E Silva and P. Cushman and T. Doughty and E. Figueroa-Feliciano and P. Kim and N. Mirabolfathi and L. Novak and R. Partridge and M. Pyle and A. Reisetter and R. Resch and B. Sadoulet and B. Serfass and K.M. Sundqvist and A. Tomada, “Validation of phonon physics in the cdms detector monte carlo,” *Journal of Low Temperature Physics*, submitted 2011.
- [52] A. Anderson, S. Leman, T. Doughty, E. Figueroa-Feliciano, K. McCarthy, M. Pyle, and B. Young, “Modeling phase-separated transition-edge sensors in supercdms detectors,” *IEEE Transactions on Applied Superconductivity*, submitted 2011.
- [53] A. Broniatowski, “A simulation code for the ionization and heat signals in low- temperature germanium detectors for dark matter research,” *Nuclear Instruments and Methods in Physics Research A* **520**, pp. 178–181, 2004.
- [54] A. Broniatowski (EDELWEISS collaboration), “Impurity scattering and electron transport anisotropy in cryogenic ge detectors for dark matter search: Monte carlo modeling and comparison to experiment,” *Journal of Low Temperature Physics*, submitted 2011.
- [55] D. Brandt, M. Asai, P. Brink, B. Cabrera, E. do Couto e Silva, M. Kelsey, S. Leman, K. McCarthy, R. Resch, and D. Wright, “Monte carlo simulation of massive absorbers for cryogenic calorimeters,” *Journal of Low Temperature Physics*, submitted 2011.